*energies*

MDPI

*Article*

# Electric Vehicle Battery-Connected Parallel Distribution Generators for Intelligent Demand Management in Smart Microgrids

**Ali M. Jasim [1,2], Basil H. Jasim [1], Bogdan-Constantin Neagu [3,*] and Simo Attila [4,*]**

[1] Electrical Engineering Department, University of Basrah, Basrah 61001, Iraq; e.alim.j.92@gmail.com (A.M.J.); hanbas632@gmail.com (B.H.J.)
[2] Department of Communications Engineering, Iraq University College, Basrah 61001, Iraq
[3] Power Engineering Department, Gheorghe Asachi Technical University of Iasi, 700050 Iasi, Romania
[4] Power Systems Department, Politehnica University Timisoara, No. 2, V. Parvan Bvd., 300223 Timisoara, Romania
* Correspondence: bogdan.neagu@tuiasi.ro (B.-C.N.); attila.simo@upt.ro (S.A.)

**Abstract:** Renewable energy penetration increases Smart Grid (SG) instability. A power balance between consumption and production can mitigate this instability. For this, intelligent and optimizing techniques can be used to properly combine and manage storage devices like Electric Vehicle Batteries (EVBs) with Demand-Side Management (DSM) strategies. The EVB helps distribution networks with auxiliary services, backup power, reliability, demand response, peak shaving, lower renewable power production's climate unpredictability, etc. In this paper, a new energy management system based on Artificial Neural Networks (ANNs) is developed to maximize the performance of islanded SG-connected EVBs. The proposed ANN controller can operate at specified periods based on the demand curve and EVB charge level to implement a peak load shaving (PLS) DSM strategy. The intelligent controller's inputs include the time of day and the EVB's State of Charge (SOC). After the controller detects a peak demand, it alerts the EVB to start delivering power. This decrease in peak demand enhances the load factor and benefits both SG investors and end users. In this study, the adopted SG includes five parallel Distribution Generators (DGs) powered by renewable resources, which are three solar Photovoltaics (PVs) and two Wind Turbines (WTs). Sharing power among these DGs ensures the SG's stability and efficiency. To fulfill demand problem-free, this study dynamically alters the power flow toward equity in power sharing using virtual impedance-based adaptive primary control level. This study proposes a decentralized robust hierarchical secondary control system employing Genetic Algorithm (GA)-optimized Proportional-Integral (PI) controller parameters with fine-grained online tuning using ANNs to restore frequency and voltage deviations. The proposed system is evidenced to be effective through MATLAB simulations and real-time data analysis on the ThingSpeak platform using internet energy technology. Our presented model not only benefits users by enhancing their utility but also reduces energy costs with robust implementation of a control structure by restoring any frequency and voltage deviations by distributing power equally among DGs regardless of demand condition variations.

**Keywords:** microgrid; distribution generators; secondary control; genetic algorithm; artificial neural network; virtual impedance; power sharing



**Citation:** Jasim, A.M.; Jasim, B.H.; Neagu, B.-C.; Attila, S. Electric Vehicle Battery-Connected Parallel Distribution Generators for Intelligent Demand Management in Smart Microgrids. *Energies* **2023**, *16*, 2570. https://doi.org/10.3390/en16062570

Academic Editors: Nima Izadyar and Valeh Moghaddam

Received: 23 January 2023
Revised: 20 February 2023
Accepted: 7 March 2023
Published: 8 March 2023



## 1. Introduction

### 1.1. Motivation

SGs are small-scale power grids made up of a collection of smart substations, integrated communications, loads, and distributed energy resources such as PV systems, WTs, diesel generators, batteries, etc. that can function autonomously or in tandem with main power grids. SGs can use multiple renewable-resource-based DGs, reduce pollution, and

boost economic benefits. The SG energy management system ensures generating and loading components perform efficiently and cost-effectively [1–4]. Most Renewable Sources (RSs) are either naturally DC or DC-friendly, making integration with a low-voltage Direct Current Transmission (DCT) system relatively simple. DCT systems appear to be an attractive option for SG distribution systems because of their superior efficiency, high reliability, and simple integration with renewable sources of energy. Since the DCT transmits only active power, its line impedances have only resistors, eliminating reactive power losses and reducing active power losses. Thus, DCT is superior to Alternating Current Transmission (ACT), while ACT can be employed near the load site for short distances following DG inverters to maximize loss benefits [1].

SG poses significant power quality challenges, particularly when an excessive number of DGs are incorporated [5]. Typically, a reliable control method is required to satisfy power quality requirements and maintain the smooth running of the SG system. Large power, voltage, and frequency variations occur in the islanded operation of SG as a result of the lack of uncertainty in the determination of the optimal gains for the controllers such as Proportional Integral (PI) controllers. Due to these issues, studies are being carried out to improve the functionality of the SG in the island mode of operation. The proportional and integral control gain coefficients need to be fine-tuned a lot to improve the performance of PI controllers [6]. Soft computing techniques can be used to make these coefficients static or dynamic throughout the process. The control gains are calculated using either the Ziegler–Nichols (Z–N) method [7,8] or an adaptive or experimental method such as "trial and error" [9–11]. Because of this, they may delay moving into a steady state of operation. During the integration of DGs and load changes, proper PI parameter tuning is essential and difficult to achieve [12]. This will ensure the improved performance of the system and power quality. Due to their dependence on operating point conditions, traditional controllers are less reliable and robust. Using intelligent learning algorithms, it is possible to overcome the technical bottlenecks. Powerful online tuning controllers have a dramatic effect on regulating secondary voltages and frequencies.

The most common method of SG control is called "droop control". Frequency–voltage droop is a popular and effective approach for managing parallel DGs. This method imitates the functioning of a power system with a predetermined droop characteristic. This wireless control method is easy to deploy and reliable since the DGs are not required to communicate. Unfortunately, it has some drawbacks that might lower performance. Its flaws include: its frequency and amplitude variations are load-dependent, leading to poor load voltage control performance; an intrinsic tradeoff between voltage regulation and power sharing across DGs; and impedance-mismatched inverters impair power-sharing performance. Therefore, when the traditional droop control scheme is used, it is impossible to avoid difficulties with insufficient power sharing. In order to maintain the stability and cost-effective functioning of the SG, the power of the DGs must be shared continuously. It is required to dynamically alter the power flow towards equity in terms of the power sharing in order to optimize the total available power to meet the demand. The aforementioned issues can be resolved by utilizing communication links with low bandwidth. By transmitting restoration signals related to each individual DG unit, a communication method with a narrow bandwidth can be adopted to improve the performance of the traditional droop method. This can be accomplished through the use of hierarchy control as a multi-level control for primary control [6].

The standard power-sharing technique is incapable of balancing a battery's SOC with varied initial values. There must be a direct connection between battery energy management and the issue of fair power sharing when integrating an energy storage source with parallel-connected DGs in SG. The optimal control and management of energy storage based on precise estimation is crucial for the reliable supply of clean, new, and renewable energy when needed. SG utility must meet time-varying peak demand [13]. Peak hours are few, so generator units are inefficient most of the time. During peak demand, generator units need more raw materials or excellent environmental conditions. Unfortunately,

wind and solar energy are not always obtainable when and where they are most needed. Furthermore, peak energy demand does not always occur during the day's windiest or sunniest hours. As a result, some utilities are struggling to meet demand because solar and wind power are insufficient during certain times of the day. Solar energy can only be collected during daylight hours. However, the highest demand for electricity occurs in the mid-evening. Electric utilities will need to keep using Battery Storage Systems (BSS) until this discrepancy is resolved. The BSS reduces the climatic variability of electrical power production in renewable unit installations. It increases renewable unit penetration, enhancing system efficiency and reliability. In addition, BSS plays an important role in distribution networks by aiding auxiliary services, backup power, demand response, peak shaving, renewable energy integration, voltage management, frequency control, and long-term and seasonal storage. If everybody started using EVBs, it would be a fantastic solution. The electric vehicle would be charged by being plugged in when it was not in use. Electric utilities have the ability to siphon power from EVBs in their entirety whenever there is a high demand for electricity. Getting people to switch to electric cars and installing charging stations in parking garages and other public areas is one way to reduce the world's excessive energy consumption. Therefore, peak load reduction has emerged as an important area of study. It permits SG utilities to reduce the peak energy production. The application of a BSS or EVB is the most desirable potential strategy for peak load reduction [14]. In this technique, PLS is accomplished by charging the BSS during periods of low demand and discharging it during periods of high demand, as depicted in Figure 1.

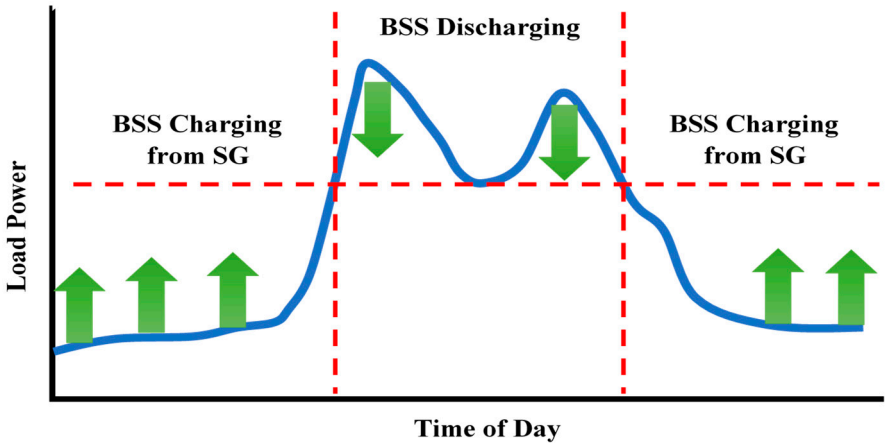


**Figure 1.** PLS using BSS, own work.

The PLS participation of EVB can optimize the daily load characteristics and improve the utilization rate of generation units, boosting the overall operating efficiency of power systems and reducing active power losses. Calculating PLS for energy storage is important for promoting its use in power production. The primary benefit of EVB-based PLS is that it enables SG utility to reduce peak demand without compromising the comfort of its customers [15]. Scheduling the charge and discharge of EVB, however, is difficult [16]. Artificial Intelligent (AI)-based battery management and lifespan prolongation solutions have garnered attention from manufacturing due to automation engineering and scientific advances. The authors of [17] proposed the capacity forecaster based on knowledge-data-driven attention (CFKDA) for Li-ion battery calendar health prognostics, which was the first study to apply the attention mechanism to battery calendar health monitoring and management. By incorporating battery empirical information in its knowledge-driven attention module, the CFKDA has improved its theoretical strength and prognostic performance. A knowledge-guided data-driven methodology forecasts battery calendar ageing [18]. Support Vector Regression (SVR) is used in this data-driven model. The mechanism and empirical information components of battery storage temperature, SOC, and time are connected to create a knowledge-guided kernel to predict battery calendar ageing trajectories

under observed circumstances. To improve generalization in unobserved settings, a classical Gaussian kernel is applied to all inputs in the knowledge-guided data-driven model. Reference [19] critically reviews current AI-based production and management solutions for long-life batteries. AI-based battery production and smart battery health are presented. The most popular AI solutions for battery-life diagnosis, including state-of-health assessment and ageing prediction, are discussed. Also shown are AI-designed battery longevity solutions. By scheduling usage of EVB, we can increase a generator's efficiency and lower its operating and maintenance costs by using PLS services [20,21].

For internet-based SG system monitoring, the Energy Internet (EI) can be widely adopted. The EI is the next step of today's internet, where objects and things have computation and communication capabilities. The EI plays a crucial role in modern society by fostering economic and social progress. Currently, the EI is being used widely in numerous industries, including those dealing with "smart cities", "smart healthcare", "smart power grids", etc. The widely used ThingSpeak platform can be adopted to generate the proposed communication structures. Users can aggregate, analyze, and visualize real-time data streams with the help of ThingSpeak, an Internet of Things (IoT) analytics platform hosted in the cloud. Using the ThingSpeak platform, users can connect their devices to the internet and create real-time data visualizations. It is able to instantly visualize data presented by the system gateways and perform online analysis and processing of data streams.

Based on the above, this paper addresses the SG issues of equal power sharing of parallel DGs, SG line losses, and demand management by using proposed intelligent control technique-based EVBs and intelligent secondary control-based parallel DGs with online tuning control parameters based on ANNs and GAs.

### *1.2. Literature Review*

Studies show that BSS and DSM are effective methods to deal with the above challenges. Because of the unpredictable and intermittent nature of RSs, DSM strategies and BSSs are essential for increasing the penetration rate of green power production by reducing short-duration variability. A number of academics for a variety of uses have studied BSS integration with renewable energy, notably peak shaving. Peak shaving is defined as discharging a battery to promote load peaks, thereby lowering the maximum electricity demand drawn from the main sources. Utility companies and homeowners alike can reap significant financial benefits from this technology. To assist the local distribution and transmission network, previous research has given several scheduling and management techniques for EVB charging. Previous studies suggest using RSs like solar PV or wind generation with energy storage to charge EVBs [20,21]. Intelligent control and scheduling algorithms that assist the electrical grid govern EVB charging. Vehicle-to-grid (V2G) technology allows EV batteries to be discharged for peak shaving or supplementary services in several of these studies [22,23]. The EVB performs well in peak load control [24] and DSM [25]. DSM was provided in [26] through distributed energy generation and storage optimization. The unpredictability and technical problems associated with the usage of high-power RSs are described, and the benefits of DSM techniques and ESSs are instigated as features to meet the existing challenges. In [27], the authors explored the significance of different BSSs for future green power systems to store and dispatch renewable power during varying scheduling periods. ESSs present novel opportunities for distribution companies to lessen the impact of using RSs by dampening power fluctuations of RSs and perfectly matched demand and supply. Battery technology may become more important for grid stability as the energy market changes [28]. A dimensioning adjustment for battery energy storage systems utilized for peak shaving based on a real-time control algorithm [29] increases peak shaving performance. In [30], an additional PLS strategy was presented that allowed for dynamic adjustments in EVB discharging rates without affecting battery usage for electric vehicle travel. This strategy reduced peak demand by putting the unused power of the grid-connected electric vehicles to use. Reference [31] compares three types of battery in a BSS controller for load leveling and peak shaving. The controller was developed using

the Matlab environment to monitor consumer load demand, and control BSS charging and discharging, while meeting load demand and extending BSS life. Reference [32] proposes a load-based peak shaving mechanism. Power load profile, battery SOC, and RS operation characteristics are considered, and an adaptive load curve-fitting method is developed. The study [33] concentrated on software that optimizes a microgrid's energy storage schedule. This schedule reduces electricity costs. Using GA or Mixed-Integer Linear Programming, an optimization technique minimizes an objective function representing electricity use information and costs. The goal of the study [34] is to produce a peak shaving algorithm for an islanded Microgrid (MG) that is based on a decision tree. The proposed algorithm assists an islanded MG in efficiently operating its generation units. DSM and a more cost-effective battery storage scale design plan for home battery storage are examined in [35].

Regarding the recent control techniques of SG, most of the published literature on decentralized secondary control of MG [36,37] provides a solution for power sharing and recovering frequency/voltage with asymptotic convergence speeds. The publishers of [38] used GA to compute the best parameters for PI and PID controllers in order to control frequency in hybrid systems. The authors of reference [39] made a PSO-based controller to set the frequency/voltage of an isolated MG. The presented controller optimized the system's dynamic behavior in terms of keeping the frequency and voltage within the specified limits. In reference [40], the PSO-based controller was made just for island MG. Even though both the source and the load changed a lot, the controller kept the frequency well within the allowable range. The authors of [41] simulated a parallel DG-based microgrid system that may be operated in island or grid-connected modes using conventional PI controllers and a virtual impedance loop. This system can correctly share power amongst parallel DGs. Reference [1] developed a secondary control strategy employing optimized PI controllers based on ANNs for accurate online parameter adjustment to address power sharing and improve SG performance. A power sharing control approach and system performance improvement in a grid-connected SG were provided by reference [42]. The control technique is based on Proportional Resonant (PR) controllers, contrasted with model predictive control and droop control. In our previous work [43], a consensus algorithm-based multi-agent system is proposed to rectify voltage/frequency deviations and allow power sharing among DGs. Each DG is considered as an agent exchanging information with its local neighbors over a sparse cyber network system. In the compensation sublayer, intelligent voltage and frequency compensators are online-adjustable PI controllers employing ANNs. This combination leverages ANN's capacity to handle parameter fluctuations and nonlinearity with the PI controller's simplicity. Table 1 provides a summary of the related previous studies.

**Table 1.** Summary of the related previous studies.

| Reference No. | Power-Sharing Control | Control Parameter Optimization | Studying Power Losses | PLS-Based DSM | Energy-Internet-Based Monitoring |
|---|---|---|---|---|---|
| [20–35] | NO | NO | NO | YES | NO |
| [36,37,39] | YES | YES | NO | NO | NO |
| [38,40] | NO | YES | NO | NO | NO |
| [1] | YES | YES | YES | NO | NO |
| [41,42] | YES | NO | NO | NO | NO |
| [43] | YES | YES | NO | NO | NO |

According to the authors' knowledge, PLS utilizing ANNs and EVBs for islanded SG was not studied until recently, and no prior research has discussed the use of decentralized secondary control with ANNs-optimized GA-based PI controllers to simultaneously restore frequency/voltage and share active/reactive power over low-voltage DCT for eliminating reactive power issues and reducing power losses.

### 1.3. Paper Contributions

Existing PLS methods of energy storage rely on precise mathematical modeling. The model of these methods is not simple enough, so machine learning tools or intelligent optimization algorithms can be used. The proposed strategy regulates EVB reference power intelligently to control charging/discharging of EVB dynamically, considering the SG load profile and EVB operation characteristics. Furthermore, with this management strategy, power sharing among DGs using decentralized secondary control with online parameter tuning by ANNs has not been studied until now. So, there is a need for an energy management software-based robust secondary control structure that effectively schedules energy storage of EVB and enhances system performance. This study concentrates on the management and control of islanded SG. In summary, the following points highlight the importance and originality of this study:

1. An innovative energy management system based on ANNs is created to maximize the performance of EVBs-connected islanded SG in zero-energy areas. The adopted SG uses RSs like solar panels and wind turbines. The proposed approach uses effective management process for intelligently managing system energy based on time of day and SOC of EVB.
2. In this paper, we propose a method for optimally controlling each DG in SG using droop, internal controllers, and decentralized secondary controllers. Moreover, the SG-connected EVB control structure consists of optimal active/reactive power and current controllers. With the proposed robust method, the voltage and frequency in the SG are both dynamically and automatically adjusted, regardless of load conditions changing.
3. To manage load variations and enhance power quality, we develop an online robust fine-tuning process based on decentralized secondary controllers with ANN learning features. ANN and GA are adopted to tune the parameters of secondary controllers in an online manner. GA determines and stores the optimal secondary PI parameters. After simulation start, an online ANN modifies the PI controller-based GA parameters simultaneously. The ANN controller's capability for learning increases the extensibility of the proposed control mechanism.
4. To meet the needs of power distribution equally among DGs, the proposed control strategy employs a virtual impedance technique based on primary control level.
5. Reduced power losses and elimination of reactive power issues motivate the adoption of the DCT transmission system for supplying power to inverters. Three-phase SG loads are typically powered by local AC transmission lines.
6. The information flow between the MATLAB program and the open-source IoT framework ThingSpeak is used in this paper to generate the proposed communication structures from the model. ThingSpeak mimics real-time cloud communication.

### 1.4. Paper Organization

The remaining sections of the paper are laid out as follows. The proposed SG framework is outlined in Section 2. The adopted SG-based renewable and storage energies are described in Section 3. Tuning PI controller parameters are presented in Section 4. EVB energy management based on intelligent ANNs controllers is discussed in Section 5. In Section 6, the decentralized intelligent secondary control of DG-based SG is described. In Section 7, the outcomes of the simulations are shown. The paper is concluded in Section 8.

## 2. Proposed SG System

The proposed islanded SG is demonstrated in Figure 2. This SG consists of five RSs (three solar PVs and two WTs), one local storage energy station, five inverters-interfaced DGs (which provide load power according to their capacity), ten DC line impedances, five AC transmission line impedances, and three loads. Hybrid solar–wind electricity is environmentally friendly. Even on overcast days or at night when solar irradiation is low, it may be erected and operated in places with ample solar and wind resources. So, this unique method will provide spectacular, and reliable electric power, departing from

hydrocarbon-based electrical energy production. Sunlight and wind may be transformed into DC or AC power. The adopted solar PVs generate DC power, whereas the WT units generate AC electricity that must be rectified into DC power via AC/DC converters. The final DC outputs are already simply applied to DC/AC inverters. Since solar–wind energy systems are unpredictable and highly dependent on weather, they need backup power sources like batteries. Thus, the EVB can alleviate some RS issues. In this work, EVB plays an important role in SG by providing backup power during peak demand periods and managing load demand using PLS strategy. EVB's PLS participation optimizes daily load characteristics, increases generating unit utilization, boosts system efficiency, and reduces active power losses. To execute the PLS DSM strategy, the proposed ANNs controller-based EVB operates at specific times depending on the demand curve and EVB charge level, which are inputs to the intelligent controller. After detecting a high demand, the controller notifies the EVB to begin supplying electricity. In the adopted SG system, DC transmission lines are adopted to transfer electricity from RSs to associated inverters because they have minimal power losses and avoid reactive power issues. DC transmission improves grid performance and protects against cascading blackouts, is environmentally friendly, and does not require reactive power compensation [41].

DC line resistances for linking the RS-based DC outputs to the related inputs of VSIs are $[R_{d1}, R_{d2}, R_{d3}, R_{d4}, R_{d5}]$. The impedances connect these DC lines with each other $[R_{d1,2}, R_{d2,3}, R_{d3,4}, R_{d4,5}, R_{d5,1}]$ are added to improve system reliability in the event of one DG power failure or for maintenance purposes. The three-phase SG loads are powered by site-specific AC transmission lines with $[R_{A1} + L_{A1}, R_{A2} + L_{A2}, R_{A3} + L_{A3}, R_{A4} + L_{A4}, R_{A5} + L_{A5}]$ impedances. Inverters, LC filters at the DG's output, and coupling impedances make up the power components of the DGs. Table 2 shows the values of all adopted SG line impedances. Figure 3 shows the DG control structure scheme. It has both primary and secondary control levels. All of this structure's observed data are in $dq$ frame. Each primary control scheme has power, current, and voltage controllers. Set points for the inverter's output frequency and voltage are set by the power control loop based on P/f and Q/V droop control characteristics. The droop coefficients are $m_p$ and $n_q$. Large droop controller slopes can speed up load sharing, but they destabilize the system. Both instantaneous active (P) and reactive (Q) power components are pumped through low-pass filters with 10 $\pi$ cutoff frequency to remove fluctuations from power calculations. To reduce the effect of line impedances and achieve proper power sharing, the virtual impedance method with (resistor = 0.03 Ω and inductor = 1.7 Ω) is used. The loops of power controller and virtual impedance create reference voltage, frequency, and line impedance's voltage drops, which are injected to voltage and current controllers to create inverter reference voltages and currents in the $dq$ reference frame. Both current and voltage controllers reduce disturbances and dampen the output filter.

**Table 2.** The SG line impedances.

| AC Line Impedance | Value (Ω + jH) | DC Line Impedance | Value (Ω) | Impedance between DC Lines | Value (Ω) |
|---|---|---|---|---|---|
| $R_{A1} + jX_{A1}$ | 0.01273 + j0.219 | $R_{d1}$ | 1 | $R_{d1,2}$ | 0.0127 |
| $R_{A2} + jX_{A2}$ | 0.0159125 + j0.2748 | $R_{d2}$ | 0.95 | $R_{d2,3}$ | 0.0317 |
| $R_{A3} + jX_{A3}$ | 0.016549 + j0.2858 | $R_{d3}$ | 0.76 | $R_{d3,4}$ | 0.0317 |
| $R_{A4} + jX_{A4}$ | 0.019095 + j0.3298 | $R_{d4}$ | 1.27 | $R_{d4,5}$ | 0.0127 |
| $R_{A5} + jX_{A5}$ | 0.014003 + j0.2419 | $R_{d5}$ | 1.14 | $R_{d5,1}$ | 0.0381 |

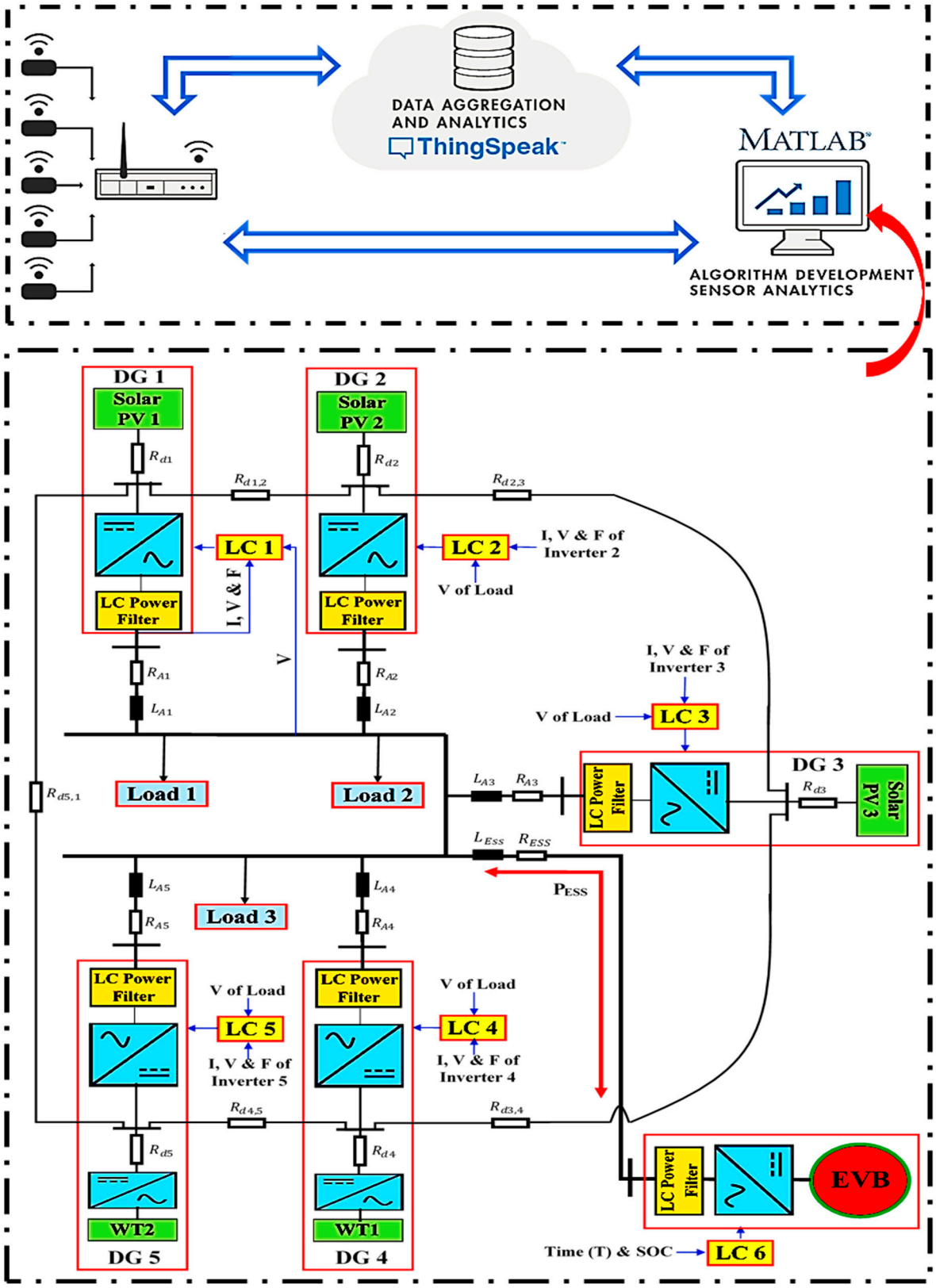


**Figure 2.** The proposed SG system, own work.

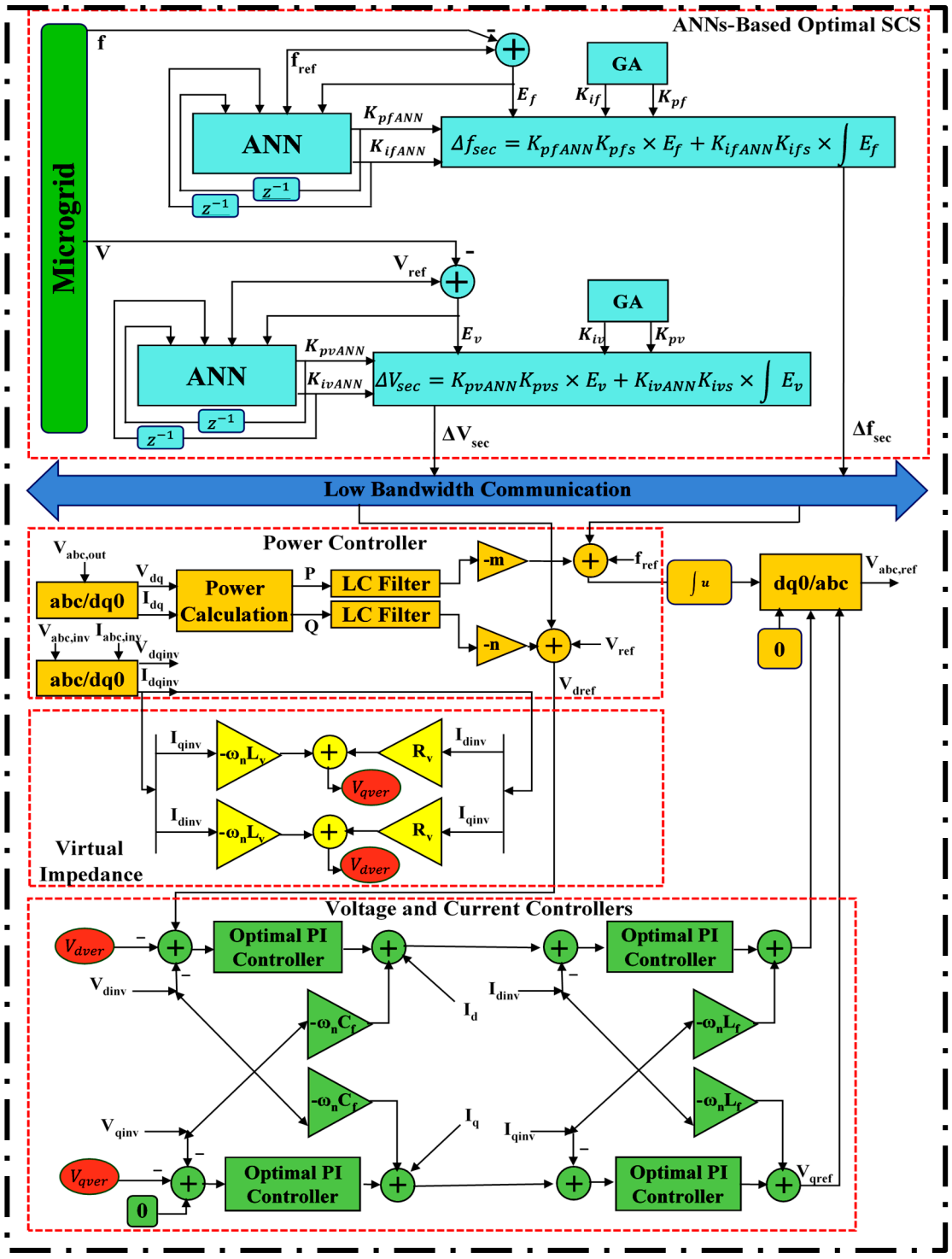


**Figure 3.** The control structure of every DG in SG, own work.

Because the droop controller cannot return the frequencies and voltages of DGs to their nominal values, secondary controllers must be used. Secondary controllers correct steady-state errors ignored by droop controllers. Figure 3 shows GA-ANN-based secondary frequency and voltage controllers for each DG. The frequency signal is instantly measured and compared to its reference value. The PI controller receives the error signal as an input and uses it to calculate the frequency deviation. A voltage signal can be controlled in a similar fashion to generate a voltage deviation. Adjusting PI controller parameters stabilizes the frequency/voltage outputs. The secondary controller is a Local Controller (LC) that

monitors load end voltage and frequency and supplements DG set-points. Secondary control signals only slightly alter reference points. Secondary units ensure SG meeting runs smoothly and without incident.

At the end, the ThingSpeak platform is proposed for real-time SG data monitoring. Remote monitoring can analyze SG data. Cloud-based IoT online analytical processing ThingSpeak aggregates, visualizes, and analyzes live data streams. MATLAB can transmit data to ThingSpeak for real-time data visualization. It can analyze online data streams and visualize gateway data.

## 3. Modeling of Renewable and Storage Energy Resources

### *3.1. Solar PV*

In Equation (1), the diode alone and the two resistors define the I–V relationship that is used to model the functioning of a PV cell [1,43]

$$I = I_{PHO} - I_{OT}(e^{(\frac{V_{SE}}{\alpha V_T})} - 1) - \frac{V_{SE}}{R_{sh}} \quad (1)$$

where $I_{PHO}$ is the photocurrent, $I_{OT}$ is the diode's reverse saturation current, $R_{sh}$ is the shunt resistor that controls the current leakage across the p-n junction, $V_{SE}$ represents the series voltage (which includes the voltage drop across the PV series resistor), and $\alpha$ is the ideality factor that shows how far the diodes are from their ideal state. $V_T$, the thermal voltage of a diode, is affected by temperature ($T$), the Boltzmann constant ($k$), the number of series-connected cells ($n$), and the electron charge (q).

$$V_T = \frac{knT}{q} \quad (2)$$

The photocurrent is a function of both the solar irradiance hitting the module and the PV cell's temperature, as shown in Equation (3).

$$I_{PHO} = \frac{GI_{PHO,n} + Gk_i\Delta T}{G_{ref}} \quad (3)$$

where $\Delta_T$ is the difference in Celsius degrees between the PV cell's actual temperature and its nominal temperature, $G_{ref}$ is the nominal irradiance, and $I_{PHO,n}$ is the photocurrent evaluated at the nominal condition (typically 25 °C temperature and 1000 Watt/m$^2$ irradiance). The temperature coefficient, $k_i$, and the solar irradiance, $G$, are both expressed in terms of watts per square meter.

The open-circuit voltage ($V_{oc}$) of the cell is temperature-dependent, as indicated by Equation (4):

$$V_{oc} = V_{oc,\,n} + k_v\Delta T \quad (4)$$

where $V_{oc,\,n}$ is the $V_{oc}$ at standard temperature and $k_v$ is the temperature coefficient for this voltage. In order to calculate the diode's saturation current, we must solve for $I_o$.

$$I_o = \frac{k_i\Delta T + I_{S,N}}{e^{(\frac{V_{oc,\,n}+k_v\Delta T}{\alpha V_T})} - 1} \quad (5)$$

where $I_{S,N}$ represents the short-circuit current under normal conditions.

### *3.2. WT Generator*

The amount of power produced by a WT is defined by Equation (6) [44]

$$P_W = 0.5A\rho C_p(\gamma, \beta)V_w^3 \quad (6)$$

where $\rho$ is air density, $A$ is swept rotor area, $C_p$ is the power coefficient which depends on the pitch angle $\beta$ and the tip speed ratio $\gamma$, and $V_W$ is wind speed.

The mathematical models used in the control system of a doubly fed induction generator are essential. The equations for the voltage developed in an induction motor with a rotating $dq$-coordinate system are as follows [43]:

$$\begin{bmatrix} v_{ds} \\ v_{qs} \\ v_{dr} \\ v_{qr} \end{bmatrix} = p \begin{bmatrix} \lambda_{ds} \\ \lambda_{qs} \\ \lambda_{dr} \\ \lambda_{qr} \end{bmatrix} + \begin{bmatrix} -\omega_1 \lambda_{ds} \\ \omega_1 \lambda_{qs} \\ -\omega_2 \lambda_{dr} \\ \omega_2 \lambda_{qr} \end{bmatrix} + \begin{bmatrix} -R_s & 0 & 0 & 0 \\ 0 & -R_s & 0 & 0 \\ 0 & 0 & R_s & 0 \\ 0 & 0 & 0 & R_s \end{bmatrix} \begin{bmatrix} i_{ds} \\ i_{qs} \\ i_{dr} \\ i_{qr} \end{bmatrix} \tag{7}$$

$$\begin{bmatrix} \lambda_{ds} \\ \lambda_{qs} \\ \lambda_{dr} \\ \lambda_{qr} \end{bmatrix} = \begin{bmatrix} -L_s & 0 & L_m & 0 \\ 0 & -L_s & 0 & L_m \\ -L_m & 0 & L_r & 0 \\ 0 & -L_m & 0 & L_r \end{bmatrix} \begin{bmatrix} i_{ds} \\ i_{qs} \\ i_{dr} \\ i_{qr} \end{bmatrix} \tag{8}$$

A dynamic equation for a doubly fed induction generator:

$$\frac{J}{n_p} \frac{d\omega_r}{dt} = T_m - n_p L_m \left( i_{qs} i_{dr} - i_{qr} i_{ds} \right) = T_m - T_{em} \tag{9}$$

where the $d$- and $q$-axes, the stator, and the rotor are indicated by the subscripts $d$, $q$, $s$, and $r$, respectively; $L$ is inductance, $\lambda$ is flux linkage, $v$ and $i$ are voltage and current, $\omega_1$ is angular synchronous speed, and $\omega_2$ is slip speed, where $\omega_2 = \omega_1 - \omega_r$. The mechanical torque is denoted by $T_m$, the rotor inductance and resistance by $L_r$ and $R_r$, the stator resistance and inductance by $R_s$ and $L_s$, the mutual inductance by $L_m$, the number of poles by $n_p$, and the rotor inertia constant by $J$.

If the stator voltage vector is used to guide the synchronously rotating $dq$-reference, this will put the $d$-axis in phase with the stator voltage vector and the $q$-axis in phase with the stator flux reference frame. Because of this, we have $\lambda_{ds} = 0$ and $\lambda_{qs} = \lambda_s$. The following equations can be found as in the stator voltage-oriented reference frame [44]:

$$i_{ds} = -\frac{L_m i_{dr}}{L_s}, \quad T_{em} = \frac{n_p \lambda_s L_m i_{dr}}{L_s} \tag{10}$$

$$\sigma = 1 - \frac{{L_m}^2}{L_s L_r} \tag{11}$$

$$v_{dr} = \sigma L_r \frac{di_{dr}}{dt} + R_r i_{dr} - (\omega_1 - \omega_r)\left( L_m i_{qs} + L_r i_{qr} \right) \tag{12}$$

$$v_{qr} = \sigma L_r \frac{di_{qr}}{dt} + R_r i_{qr} + (\omega_1 - \omega_r)(L_m i_{ds} + L_r i_{dr}) \tag{13}$$

### *3.3. Energy Storage System*

Terminal voltage and SOC are both useful indicators of battery health in a BSS [1,43–47]:

$$V_o = R.e^{B \int i_b dt} + R_b i_b + V_b - K \frac{Q}{Q + \int i_b dt} \tag{14}$$

$$SOC = \frac{\int 100 i_b dt}{Q} + 100 \tag{15}$$

where $R_b$ represents the battery's internal resistance BESS charging current ($i_b$), $K$ represents the polarization voltage, and the open-circuit voltage is $V_o$. Battery capacity ($Q$), exponential voltage ($R$), and total storage capacity ($B$) are all symbols used to describe the same thing.

## 4. PI Controllers' Parameter Tuning

Every DG necessitates dual internal controllers to manage primary control level-based voltage and current feedback signals. Frequency and voltage deviations, as well as power-sharing issues, are exacerbated by primary control. Because of this, the DG requires secondary control to compensate for frequency and voltage signal deviations. Every controller in both primary and secondary levels has proportional and integral gain coefficients. There are two controllers for current and voltage loops in the primary level. At the secondary level, there are also frequency and voltage loop controllers. Moreover, the EVB control technique requires two PI controllers for power and current loops. Therefore, we require twelve control coefficients. Using evolutionary algorithms like GA allows for parameter tuning across a broader usable range. The speed of convergence is slow for the standard GA, which is not an important factor in our work. GA has better global convergence than PSO, but PSO is easier and more flexible. The main problem with PSO is that it often results in premature convergence since it is difficult to fine-tune the velocity step size in the search space [48]. GAs can process multiple strings at once. In this way, the search space is thoroughly investigated. Results are more reliable, and the risk of falling into a local minimum is greatly diminished [49].

By incorporating GA into the proposed control system, the scope of the initial search is narrowed. We determine a suitable range to offer sufficient freedom for the GA and a satisfactory control procedure based on the ranges of control parameters. The chromosome in this model is a string with ten genes. In order to get the desired readings for the frequency and voltage signals again, the following objective function ($O.F$) is applied.

$$O.F = \sqrt{\left\{\sum_{n=1}^{N}\left(k_{vl}\left|\left(\left(\sqrt{|v_{dLoad}(n)|^2+\left|v_{qLoad}(n)\right|^2}\right)-v_{nomAC}(n)\right)\right|\right)^2\right\}+\left\{\sum_{n=1}^{N}k_f|f_{nom}(n)-f(n)|^2\right\}+\left\{\sum_{n=1}^{N}k_{vo}|vo(n)|^2\right\}} \quad (16)$$

where $N$ is the simulation time samples, $n$ is the sample number, $v_{dLoad}$ and $v_{qLoad}$ are the $dq$ load voltage components, $v_{nomAC}$ is the SG system's nominal AC voltage, and $f_{nom}$ and $f$ are the system's nominal and measured frequencies. In addition, $vo$ is the inverter output voltage. The proposed system operates at a low voltage, 50 Hz, 220 V. Voltage deviations are 11 V (5% of 220), and frequency deviations are 0.5 Hz (1% of 50). Table 3 lists the GA-based offline control parameter tuning. Figure 4 shows the flowchart of GA-based optimization. The convergence curve of the GA is illustrated in Figure 5. The objective function optimizes control parameters after initialization. As a result, the optimal control parameters indicated in Table 3 are achieved, where [$K_{pi}$ $K_{ii}$] are the proportional and integral parameter gains of the primary current controller, [$K_{pv}$ $K_{iv}$] are the proportional and integral parameter gains of the primary voltage controller, [$K_{pvs}$ $K_{ivs}$] are the voltage controller parameters of the Secondary Control Unit (SCU), and [$K_{pfs}$ $K_{ifs}$] are the frequency controller parameters of SCU. EVB-based load management structure power and current controller parameters are [$K_{pP}$ $K_{iP}$] and [$K_{pC}$ $K_{iC}$]. Since this is the initial offline step of the proposed approach, a slow convergence time may provide superior control settings. By defining the GA settings as number population = 15, generation number = 55, lower limit = 0, higher limit = [$K_{pv}$ $K_{iv}$ $K_{pi}$ $K_{ii}$ $K_{pvs}$ $K_{ivs}$ $K_{pfs}$ $K_{ifs}$ $K_{pP}$ $K_{iP}$ $K_{pC}$ $K_{iC}$] = [10 2000 1000 5 0.2 0.2 5 10 10 100 5 100], simulation time = 5.5 s. After sorting the population to find members with the lowest voltage and frequency differences, crossover and mutation operators produce a new generation. Since the @gaoptimset function has been utilized, the mutation operator used by default is @mutationadaptfeasible. As the suggested mutation function for restricted minimization problems, @mutationadaptfeasible is used. The specified default mutation function creates randomly adaptable directions relative to the previous successful or failed generation. Mutation follows boundaries and linear restrictions. CrossoverFraction is changed between the values 0 and 1. A crossover

percentage of n indicates that, among all non-elite offspring, n percent of the children in the future generation will be the result of crossover, while the remainder will be the product of mutation. Crossover uses the 0.6 fraction. If the termination criterion is met, the optimal control parameters are determined. The elapsed time calculated to obtain the optimal values is 31,998 s.

**Table 3.** The control parameter values using GA.

| AC Line Impedance | Value |
|---|---|
| Outer voltage controller proportional gain ($K_{pv}$) | 7.56 |
| Outer voltage controller integral gain ($K_{iv}$) | 1838 |
| Inner current controller proportional gain ($K_{pi}$) | 462.3 |
| Inner current controller integral gain ($K_{ii}$) | 3 |
| Secondary voltage controller proportional gain ($K_{pvs}$) | 0.086 |
| Secondary voltage controller integral gain ($K_{ivs}$) | 0.16 |
| Secondary frequency controller proportional gain ($K_{pfs}$) | 2.19 |
| Secondary frequency controller integral gain ($K_{ifs}$) | 7.38 |
| Battery power controller proportional gain ($K_{pP}$) | 9.1 |
| Battery power controller integral gain ($K_{iP}$) | 67 |
| Battery current controller proportional gain ($K_{pC}$) | 4.4 |
| Battery current controller integral gain ($K_{iC}$) | 99 |

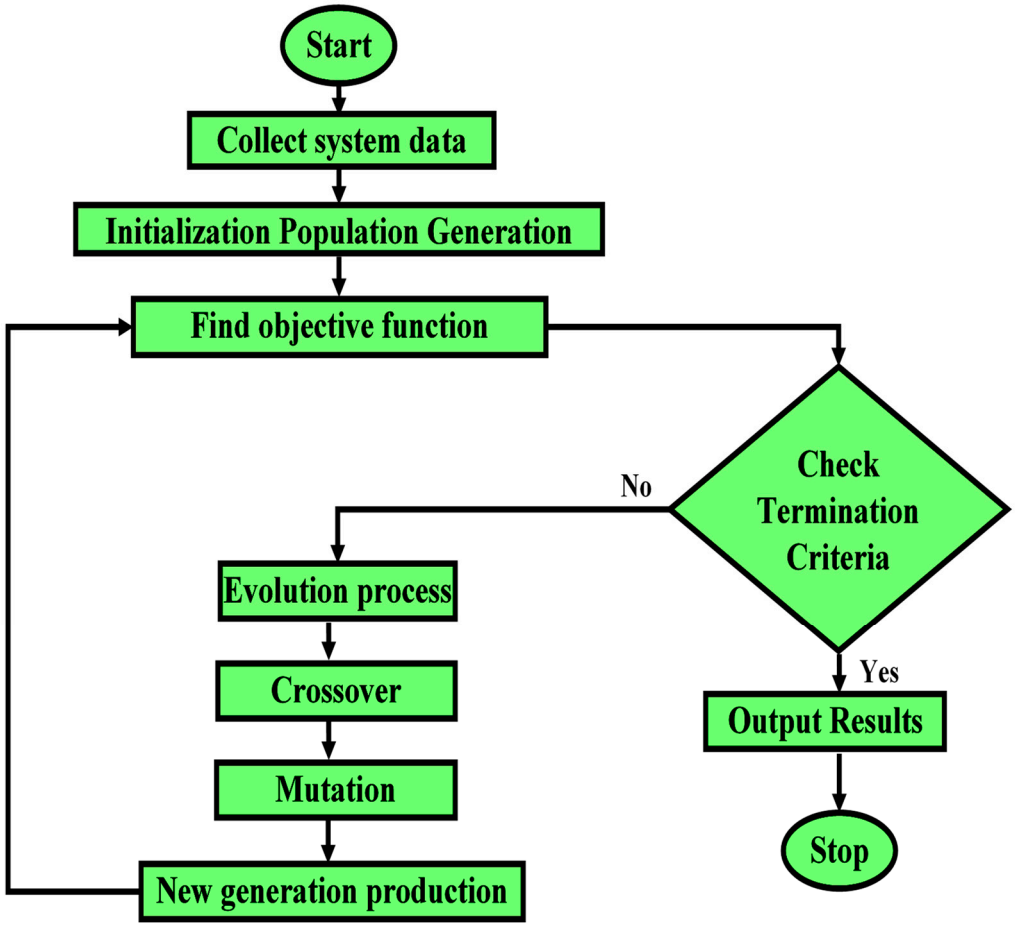


**Figure 4.** GA-based optimization flowchart, own work, based on [1].

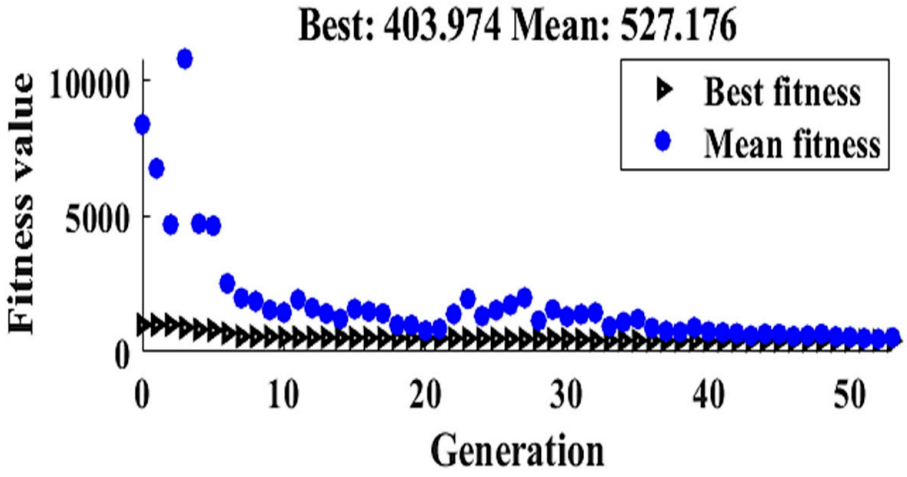


**Figure 5.** Convergence curve of the GA, own work.

In this research, the proposed system is "robust" because when we ran it twenty times, the intended results were always the same and the standard deviations (the variation from the mean value) of the control parameter values were extremely small. The standard deviation values of optimization-based parameters are [$K_{pv}$ $K_{iv}$ $K_{pi}$ $K_{ii}$ $K_{pvs}$ $K_{ivs}$ $K_{pfs}$ $K_{ifs}$ $K_{pP}$ $K_{iP}$ $K_{pC}$ $K_{iC}$] = [0.1 3 1.1 0.1 0.001 0.005 0.08 0.11 0.12 0.25 0.05 0.3]. Furthermore, these values of the optimization algorithm's parameters are not to be finally adopted in the proposed system, since the system employs ANN to alter the system's parameters in real time with more precision. We develop an ANN-based SCU that interacts with a GA-optimized PI controller as shown in Figure 3. To maintain the nominal set-points of both voltage and frequency online, the GA must adjust initial process parameters. MG voltage and frequency could collapse if the control action is ineffective. To prevent this, we use ANN-based SG decentralized SCU. The presented SCUs based on ANNs adjust parameters online, which broadens the method's applicability. The studied system collects voltage and frequency data. These inputs are used by an ANN to adjust the weights of its nodes. All DGs have accurate set-points. This risk-free control operation guarantees constant SG voltage and frequency.

According to the system expert, the ANN-based controller will have 5 neurons in the input layer and 20 neurons in the hidden layer. Input layer neurons are linear, but hidden layer neurons are nonlinear. Nonlinearity allows smooth weight changes. The number of control variables determines output-layer neurons. Figure 2 shows that the investigated SG has five DGs. Each DG has voltage and frequency controllers. Each secondary controller has proportional and integral gains. The output layer has two linear neurons per controller.

A neuron is the basic building block of ANN, and it has three parts: weights, bias, and activation function $f(net)$. Equation (17) describes the relationship of these parameters [50].

$$y_j^p = net_j^p = f\left(\sum_{i=1}^{n} x_i^p w_{ij}^p - \theta_i\right) \tag{17}$$

where $x_i^p$ denotes incoming data at iteration $p$, $n$ denotes input-layer neurons, and $w_{ij}^p$ denotes hidden-layer weights; $f(net)$ can be logsigmoid, sign, etc. The back-propagation algorithm requires activation function derivatives $(f'(net))$.

The differential of the hidden layer's activation function is given by

$$f'\left(net_j^p\right) = f\left(net_j^p\right)\left[1 - f\left(net_j^p\right)\right] \tag{18}$$

The nodes of the output layer are calculated using

$$y_k^p = net_k^p = f\left(\sum_{j=1}^{Q} y_j^p w_{jk}^p - \theta_j\right) \quad k = 1, 2 \tag{19}$$

where $Q$ is the hidden layer's neurons and $w_{jk}^{p}$ is its weight vector. To calculate a PI controller's two parameters, use the following equations:

$$K_P^p = O_1^p \tag{20}$$

$$K_i^p = O_2^p \tag{21}$$

The input vector activates the output and hidden layers in feed-forward. The primary goal of the ANN structure is to minimize frequency and voltage deviations, thereby enhancing the MG's stability. This study's feedback procedure uses supervised learning. The learning approach uses back-propagation. The proposed learning process reduces the error signal to optimize. The neuron $k$ and $p$ iteration error function is [50]:

$$e_k^p = yd_k^p - y_k^p \tag{22}$$

where $y_k^p$ and $yd_k^p$ are measured and desired outputs. Voltage and frequency desired values are [220 V 50 Hz]. The weights are updated using the error signal ($e_k^p$) as follows:

$$w_{jk}^{p+1} = w_{jk}^p + \Delta w_{jk}^p \tag{23}$$

$$w_{ij}^{p+1} = w_{ij}^p + \Delta w_{ij}^p \tag{24}$$

where $\Delta w_{ij}^p$ and $\Delta w_{jk}^p$ are system error weight changes and $i$, $j$, and $k$ indicate input, hidden, and output neurons.

$$\Delta w_{jk}^p = \eta y_j^p \delta_k^p \tag{25}$$

where a small positive constant ($\eta$) is the learning rate and $\delta_k^p$ is the error gradient in neuron $k$ in the output layer at iteration $p$.

An error gradient is set up when the derivative of the activation function is multiplied by the error at the neuron's output. Because of this, for neuron $k$ in the output layer, we have

$$\delta_k^p = \frac{\partial y_k^p}{\partial X_k^p} e_k^p \tag{26}$$

where the net weighted input to neuron $k$ during the same iteration in the process is represented by $X_k^p$. Specifically, for a sigmoid activation function, Equation (26) can be written as:

$$\delta_k^p = \frac{\partial \left\{ \frac{1}{1+e^{-X_k^p}} \right\}}{\partial X_k^p} e_k^p = \frac{e^{-X_k^p}}{\left\{ 1 + e^{-X_k^p} \right\}^2} e_k^p \tag{27}$$

Therefore, we obtain:

$$\delta_k^p = y_k^p \left( 1 - y_k^p \right) e_k^p \tag{28}$$

where,

$$y_k^p = \frac{1}{1 + e^{-X_k^p}} \tag{29}$$

The hidden-layer weight update can be calculated using the same equation as the output layer:

$$\Delta w_{ij}^p = \eta x_i^p \delta_j^p \tag{30}$$

where $\delta_j^p$ is the hidden-layer $j$ neuron's error gradient.

$$\delta_j^p = y_j^p \left\{ 1 - y_j^p \right\} \times \sum_{k=1}^{R} \delta_k^p w_{jk}^p \tag{31}$$

where $R$ represents the total number of neurons in the target layer's output.

$$y_j^p = \frac{1}{1 + e^{-\sum_{i=1}^{n} x_i^p w_{ij}^p - \theta_j}} \tag{32}$$

The training procedure will proceed until the absolute minimum of errors is achieved.

Both the ANN- and GA-based PI secondary frequency and voltage controllers have two secondary outputs. With the proposed controllers, we can adjust the frequency with their outputs $[K_{pfANN}\ K_{ifANN}]$ and $[K_{pfs}K_{ifs}]$. The parameters $[K_{pvANN}\ K_{ivANN}]$ and $[K_{pvs}K_{ivs}]$ for controlling the voltage are similar.

$$\Delta V_{sec} = K_{pvANN}K_{pvs} \times E_v + K_{ivANN}K_{ivs} \times \int E_v \tag{33}$$

$$\Delta f_{sec} = K_{pfANN}K_{pfs} \times E_f + K_{ifANN}K_{ifs} \times \int E_f \tag{34}$$

where $E_v$ and $E_f$ are voltage and frequency error signals. The deviation between the target and actual values is expressed by the error signal.

## 5. Intelligent ANN-Controller-Based EVB Energy Management

Batteries are becoming one of the most essential energy storage options due to the transition to renewable energy. Battery management is crucial for efficient, safe, and long-lasting function. Yet, the regularly changing load and operating circumstances, etc., provide obstacles for conventional battery management. Under witnessed and unwitnessed storage circumstances, study [51] presents a transferred recurrent NN-based architecture for calendar capacity prognostics. A base model and transfer model make up this transferred recurrent ANN structure. Transfer learning was used for battery state assessment and ageing prognostics in the article [52]. Conventional battery management's general concerns and transfer learning's solutions are highlighted. Next, the unique issues of each subject are identified and transfer-learning-based solutions are discussed, followed by a review of the state of the art in terms of concepts, algorithm frameworks, benefits, and limitations. Moreover, high RS penetration and decentralization have increased system instability. To reduce instability, a balance must be maintained between consumption demand and production rate. ANNs can be used to integrate EVBs with demand-side management. This paper develops an ANN-based energy management system for SG-connected EVB. ANNs are adopted to schedule power from EVB from/to SG in order to increase the system's reliability, maintain the supply–demand balance, and reduce system power losses during peak demand hours. Information about the battery's charge level and the demand curve can be used to set the controller's timing for peak and off-peak hours. The flowchart of the training process of ANN-based battery control is shown in Figure 6. As illustrated in Figure 6, the ANN-controller-based EVB generates the reference power ($P_{ref,ESS}$) for its control unit depending on various time-of-day periods and battery SOC situations.

The intelligent controller's inputs are time of day and SOC of EVB. During normal operating hours, the SG meets all load power requirements and charging EVB (charging mode). Once the ANN controller detects a peak, it notifies the EVB to begin supplying the building's appliances with energy (discharging mode). Running the EVB during peak hours lowers the peak-to-average power ratio, allowing appliances to run more efficiently and reducing active power losses. During the SG's off-peak hours, this depleted EVB will be fully recharged. By discharging ESSs during peak demand hours and charging them during off-peak hours, the proposed peak-shaving-based technique lowers peak consumption, saves demand power, and maintains supply–demand balance.

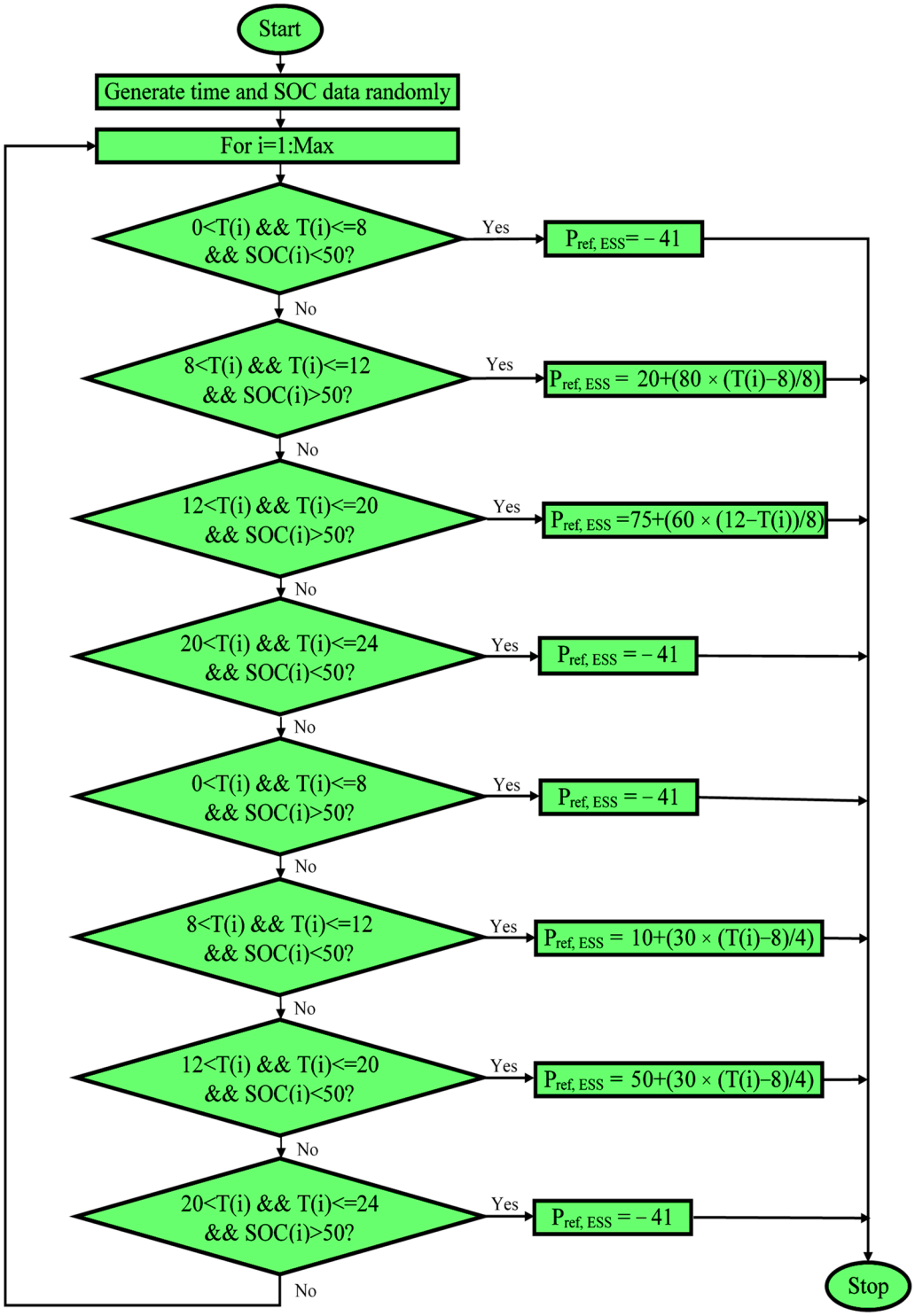


**Figure 6.** The flowchart of the proposed training process of ANN-based battery control, own work.

Figure 7 illustrates the overall optimal PQ control technique of EVB using PI controllers. Each PI controller in the *dq* axes is primarily controlled independently using the PQ control technique for managing active/reactive power. The GA is adopted to optimize the PI controller parameters. Two of the four PI controllers are outer controllers to regulate active (P) and reactive (Q) powers, while the other two are inner current controllers to control battery inverter stability and reduce harmonics. The outputs of active and reactive PI controllers

are the reference $dq$ currents ($I_{dref}$ and $I_{qref}$) that are applied to the current controllers. The formulae for the power controllers are represented by Equations (35) and (36), respectively.

$$I_{dref} = K_{pP} \times \left(P_{ref,ESS} - P\right) + K_{iP} \times \int \left(P_{ref,ESS} - P\right) \tag{35}$$

$$I_{qref} = K_{pP} \times \left(Q - Q_{ref}\right) + K_{iP} \times \int \left(Q - Q_{ref}\right) \tag{36}$$

where $P_{ref,ESS}$ and $Q_{ref}$ are the reference active and reactive powers, respectively.

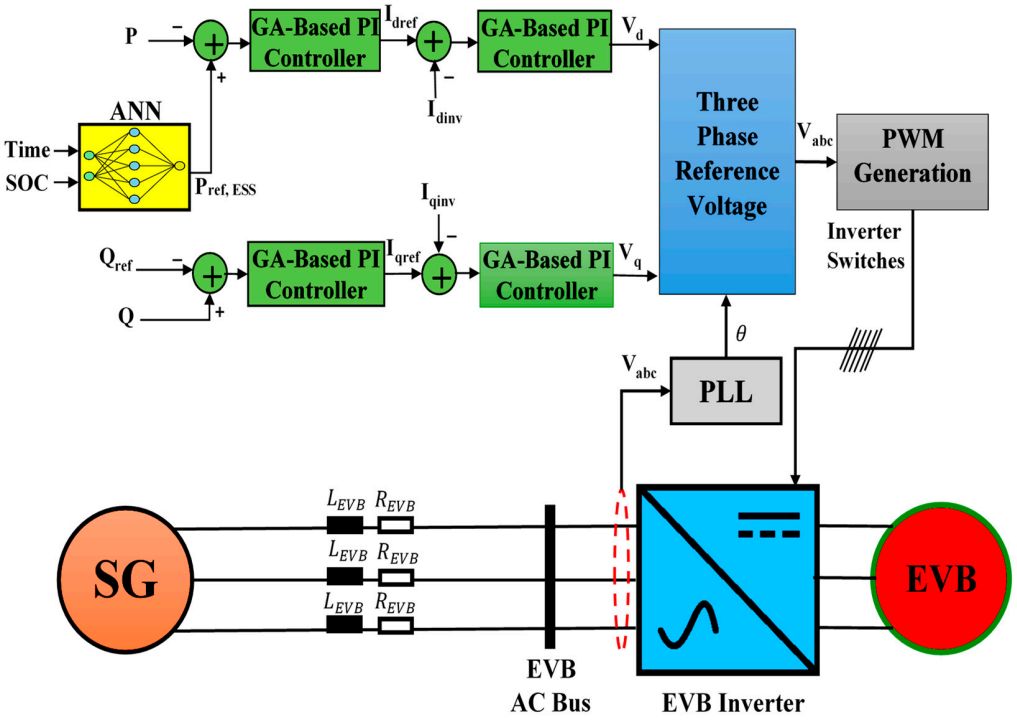


**Figure 7.** The overall optimal EVB PQ control technique using PI controllers, own work.

The periodic three-phase voltages ($V_a$, $V_b$, $V_c$) and currents ($I_a$, $I_b$, $I_c$) are associated with 3 ph instantaneous active power and reactive power. These formulae are used in the calculations:

$$P = V_a \times I_a + V_b \times I_b + V_c \times I_c \tag{37}$$

$$Q = \frac{1}{\sqrt{3}}[(V_b - V_c) \times I_a + (V_c - V_a) \times I_b + (V_a - V_c) \times I_c] \tag{38}$$

As can be seen in Figure 7, the primary feature of the optimal current controllers is their ability to regulate the $dq$ axes current component, thereby adjusting the active and reactive power of the EVB. The outputs of these outer controllers are the voltages in the $dq$ frame.

$$V_d = K_{pC} \times \left(I_{dref} - I_{dinv}\right) + K_{iC} \times \int \left(I_{dref} - I_{dinv}\right) \tag{39}$$

$$V_q = K_{pC} \times \left(I_{qref} - I_{qinv}\right) + K_{iC} \times \int \left(I_{qref} - I_{qinv}\right) \tag{40}$$

A Phase-Locked Loop (PLL) is employed to compute the voltage angle, with the resulting voltage signals being fed into a reference system for the purpose of defining the transformation between the $dq$ frame and $abc$ frame. Using the $abc$ final generation voltage, the PWM signals for the switching inverter are generated.

## 6. Decentralized Intelligent Secondary Control of DG-Based SG

Parallel inverters are managed via frequency–voltage droop. Sadly, it contains various flaws that might reduce performance. Its disadvantages include load-dependent frequency and amplitude changes, a built-in tradeoff between voltage regulation and DG power sharing, and impedance mismatched inverters that reduce power-sharing performance. The SG's stability and cost-effectiveness depend on DG power sharing. The standard droop control approach cannot prevent power-sharing issues. To optimize power supply to match demand, power flow must be dynamically adjusted toward equity. This study introduces optimization-based intelligent secondary control for power sharing. In this control technique, each DG unit has an intelligent, decentralized SCU to correct voltage and frequency abnormalities and make sure the deployed parallel DGs are effectively sharing load power. As illustrated in Figure 3, Equations (41) and (42) represent the power controller's outputs:

$$\omega = \omega_{ref} - mP + \Delta f_{sec} \tag{41}$$

$$V_{dref} = V_{ref} - nQ + \Delta V_{sec}\ ,\ V_{dref} = 0 \tag{42}$$

where $\omega$ represents the measured frequency (rad/sec.); the active and reactive power of a given DG are represented by the $P$ and $Q$ signals, respectively; $V_{ref}$ and ($\omega_{ref}$ or $\omega_n$) represent the reference values of the SG voltage and frequency; $\Delta f_{sec}$ and $\Delta V_{sec}$ denote the deviations of frequency and voltage (outputs of the SCUs); and $V_{dref}$ and $V_{qref}$ denote the reference voltages in the dq-frame.

To reduce voltage and frequency variations, supplementary outputs are added to the usual droop equations. Using Equations (43) and (44), virtual impedance circuits have been incorporated into the main control to guarantee that the DGs distribute the load power equitably.

$$V_{dver} = R_v I_d - \omega_{ref} L_v I_q \tag{43}$$

$$V_{qver} = R_v I_q - \omega_{ref} L_v I_d \tag{44}$$

where $R_v$ and $L_v$ represent the virtual resistance and the inductance, $I_d$ and $I_q$ represent inverter measured currents in the $dq$-frame, and $V_{dver}$ and $V_{qver}$ represent the compensation voltages for droop voltages caused by mismatched line impedances.

$I_{dref}$ and $I_{qref}$, which are reference dq-frame currents, are supplied to the internal current controller via the exterior voltage controller using Equations (45) and (46).

$$I_{dref} = \left\{ K_{pv}\left(V_{dref} - V_{dinv} - V_{dver}\right) + K_{iv}\int\left(V_{dref} - V_{dinv} - V_{dver}\right)\right\} + I_d - \omega_{ref} C_f V_{qinv} \tag{45}$$

$$I_{qref} = \left\{ K_{pv}\left(V_{qref} - V_{qinv} - V_{qver}\right) + K_{iv}\int\left(V_{qref} - V_{qinv} - V_{qver}\right)\right\} + I_d - \omega_{ref} C_f V_{dinv} \tag{46}$$

where $V_{qinv}$ and $V_{dinv}$ denote the inverter measured voltages in the $dq$-frame inverter, $\omega_{ref} C_f V_{qinv}$ and $\omega_{ref} C_f V_{dinv}$ denote the cross-decoupled variables used to regulate the voltage independently along the dq axis, and $C_f$ represents the capacitor of the inverter power filter.

The internal current controller uses Equations (47) and (48) to generate the reference inverter voltage in the $dq$-frame:

$$V_{dref,inv} = \left\{ K_{pi}\left(I_{dref} - I_d\right) + K_{ii}\int\left(I_{dref} - I_d\right)\right\} - \omega_{ref} L_f I_q \tag{47}$$

$$V_{qref,inv} = \left\{ K_{pi}\left(I_{qref} - I_q\right) + K_{ii}\int\left(I_{qref} - I_q\right)\right\} - \omega_{ref} L_f I_d \tag{48}$$

where $\omega_{ref} L_f I_d$ and $\omega_{ref} L_f I_q$ denote the cross-decoupled values utilized to individually regulate the current along the dq axis. Lastly, $L_f$ is the inductor of the inverter power filter.

The inverse Park transformation is then applied to the dq0-frame reference voltage values to convert them to the abc-frame representation:

$$\begin{bmatrix} V_a \\ V_b \\ V_c \end{bmatrix} = \begin{bmatrix} \cos(\omega t) & -\sin(\omega t) & 1 \\ \cos\left(-\frac{2\pi}{3} + \omega t\right) & -\sin\left(-\frac{2\pi}{3} + \omega t\right) & 1 \\ \cos\left(\frac{2\pi}{3} + \omega t\right) & -sin\left(-\frac{2\pi}{3} + \omega t\right) & 1 \end{bmatrix} \begin{bmatrix} V_{dref,inv} \\ V_{qref,inv} \\ 0 \end{bmatrix} \quad (49)$$

To activate the associated VSI's power electronics switches, these three-phase signals are fed into a Pulse Width Modulation (PWM) generator.

## 7. Simulation Results

To assess the performance of the suggested control structure, the proposed islanded SG, shown in Figure 2, is executed under load response variations based on EVB. After applying load management to the SG, frequency and voltage profiles, sharing the load power, and system losses are observed.

### *7.1. EVB-Based Load Management Results*

Figure 8 illustrates the total load profile (green curve) with a maximum consumption power of 182 kW. This curve is the summation of all adopted individual SG loads (load1, load2, load3, and static load). Figure 9 demonstrates the SG power generation curve as well as the EVB power curve. It is interpreted that during peak times, the load draws power from EVB in addition to SG power generation. Consequently, as depicted in Figure 10, the peak power requirement is reduced. During peak hours, the load demand and SG generation are reduced from 182 kW to below 150 kW. Solar and wind power are not always available when they are needed. In addition, energy may not be required during sunny or windy weather. The most electricity is used in the early mid-evening. Until this problem is fixed, electric utilities cannot stop using BSS. As Figure 10 shows, the answer is to use stored energy. EVBs would be a great solution if everyone used them. When electric cars are not being used, they would be plugged into a power source. When there is a lot of demand for electricity, electric utilities could take power from all EVBs. High energy use can be solved by convincing people to buy electric cars and installing charging stations in parking lots. The SOC level of the EVB is demonstrated in Figure 11. In the peak demand hours, the BEV continues to discharge (from hour = 8 to hour = 20). The power can be stored in batteries during periods of low demand and then released to meet load during times of high peak demand. As a result, the system's performance is enhanced, and its reliance on SG generation resources is reduced.

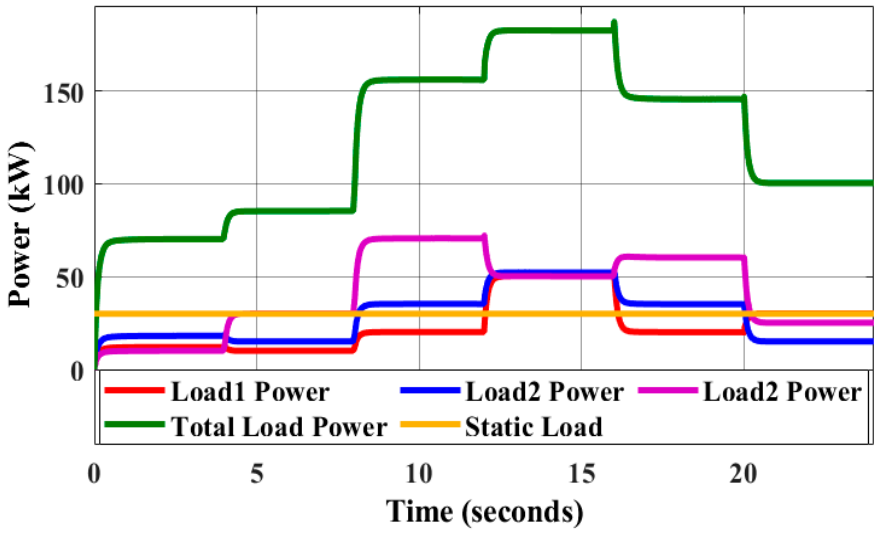


**Figure 8.** The total SG load and individual load curves.

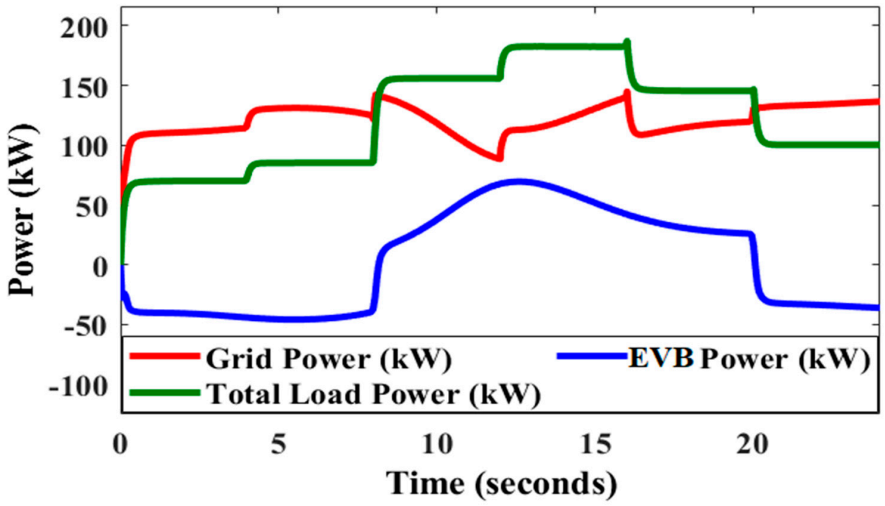


**Figure 9.** The SG power generation, load profile, and EVB output.

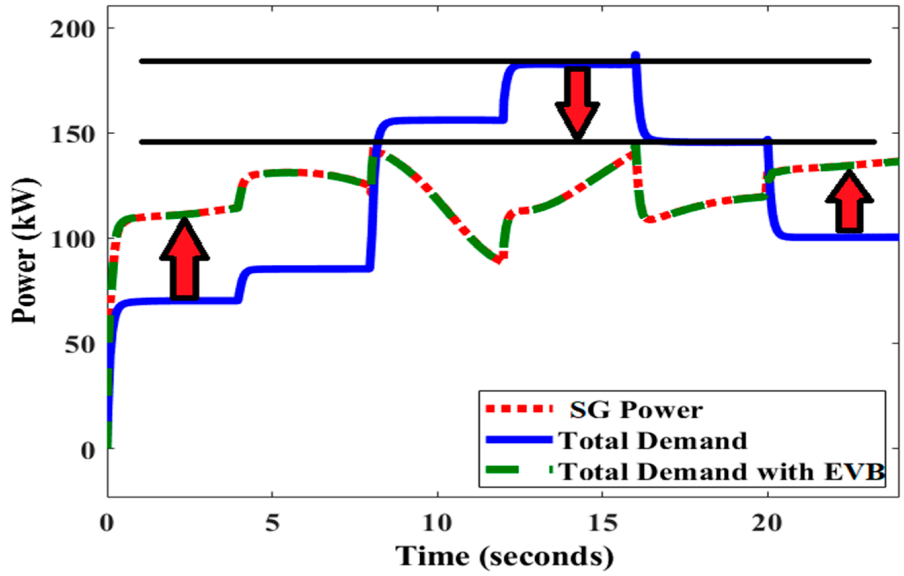


**Figure 10.** Total SG power generation and demand with and without EVB.

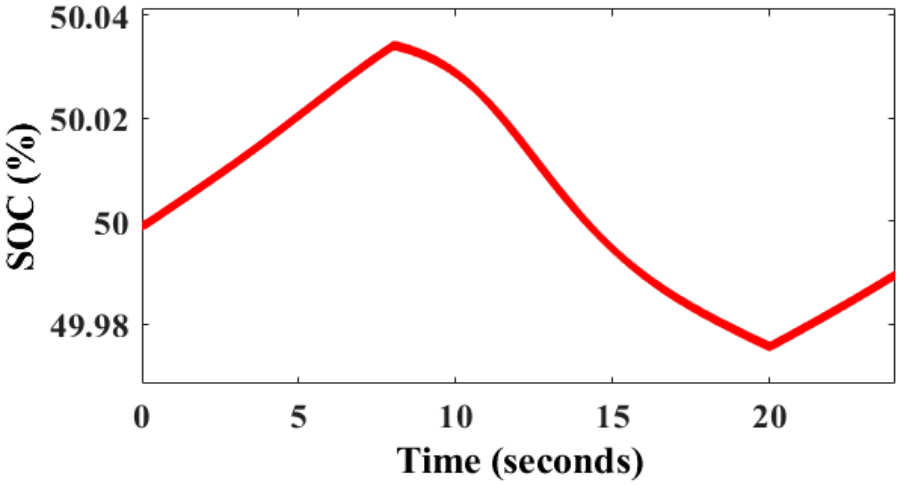


**Figure 11.** SOC level of EVB.

### *7.2. Voltage/Frequency Deviations Restoration and Power-Sharing Results*

The proposed technique has the expected performance in terms of minimizing voltage and frequency deviations when the load changes. Each DG's voltage and frequency is shown in Figure 12a,b, respectively. The proposed control technique is shown to be resistant to fluctuations in the load. After some adjusting, the voltage and frequency have reached their standard settings (50 Hz and 220 V). The frequency and voltage deviations are illustrated in Figure 13a,b, respectively. The proposed secondary control level serves to compensate for these deviations. Results of the proposed methods for active power sharing are shown in Figure 14. Adopting the proposed control structure based on virtual impedance ensures that the five DGs are in balance with respect to transient and steady-state load sharing, and that all inverters are in phase with one another. Therefore, the number of adopted DGs equally divides the power demand at any load step change by five. Figure 15 displays the update curves for these control system parameters across all SCUs. These results show that ANN-based SCUs adjust the control parameters of all DGs to ensure that stable voltage and frequency profiles are achieved. Figure 16 illustrates the voltage and current signals for the AC bus. It is found that voltage signals are sinusoidal with constant amplitude regardless of load changes, whereas the amplitude of current signals varies in response to load changes. The root-mean-square values of these signals are illustrated in Figure 17.

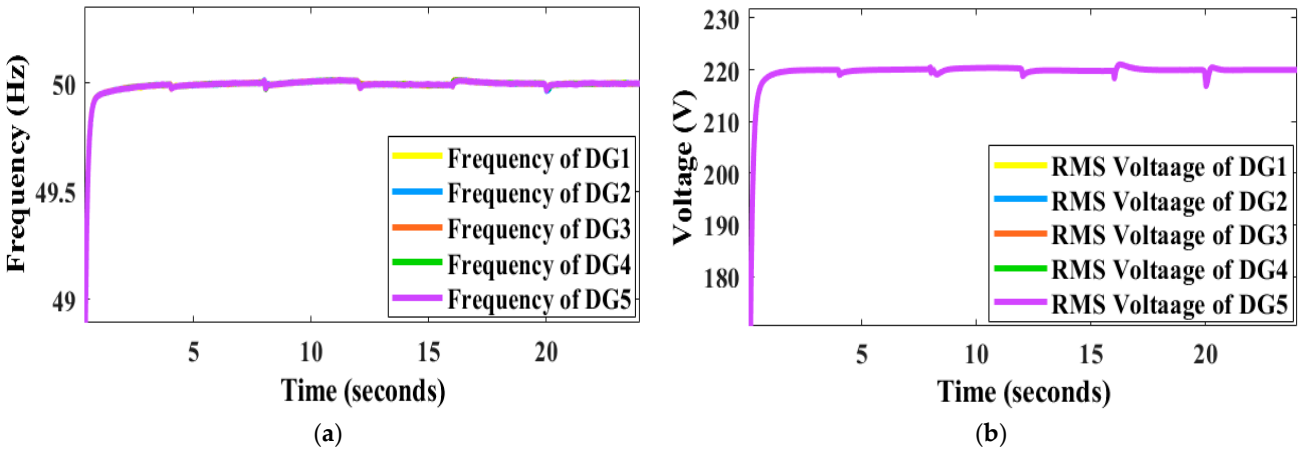


**Figure 12.** (**a**) Frequency and (**b**) voltage patterns of all DGs as the load changes.

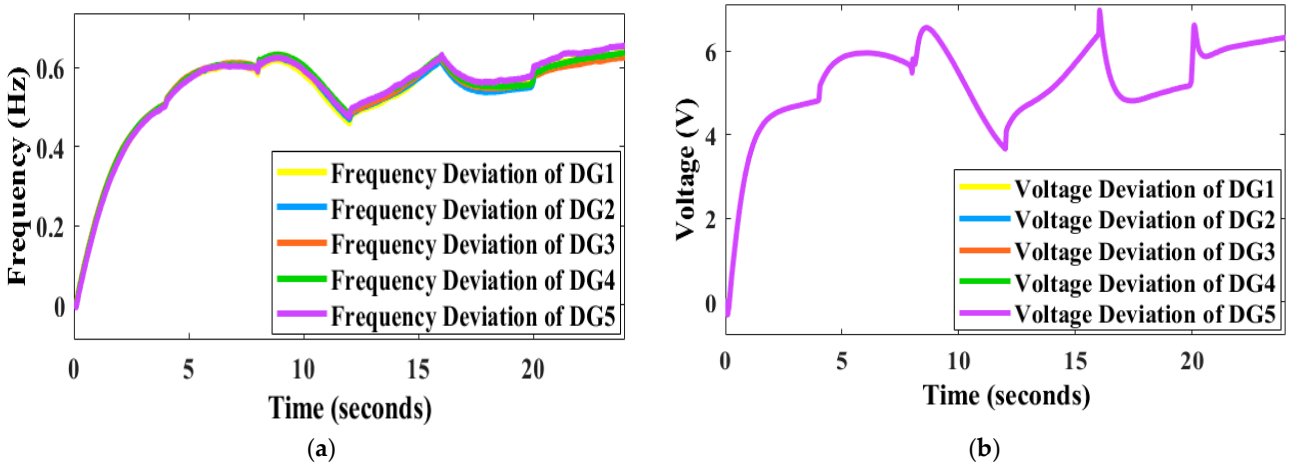


**Figure 13.** (**a**) Frequency deviation and (**b**) voltage deviation patterns of all DGs as the load changes.

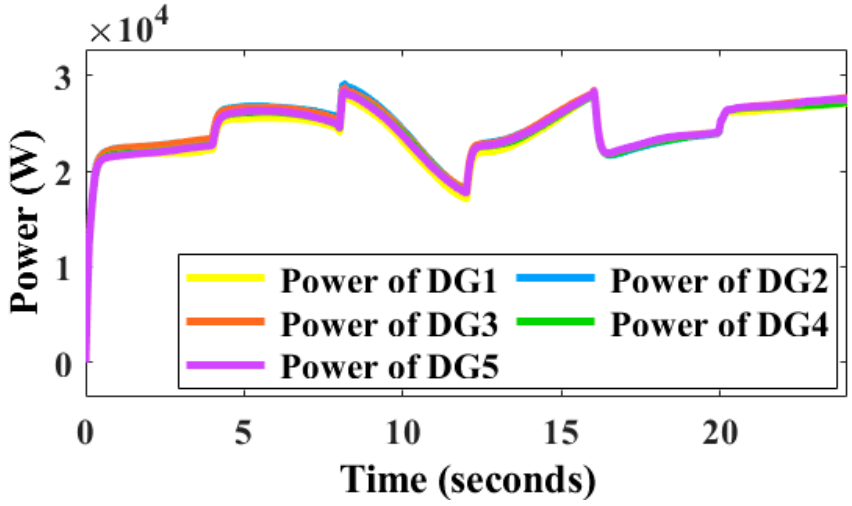


**Figure 14.** Output power of all DGs as load conditions change.

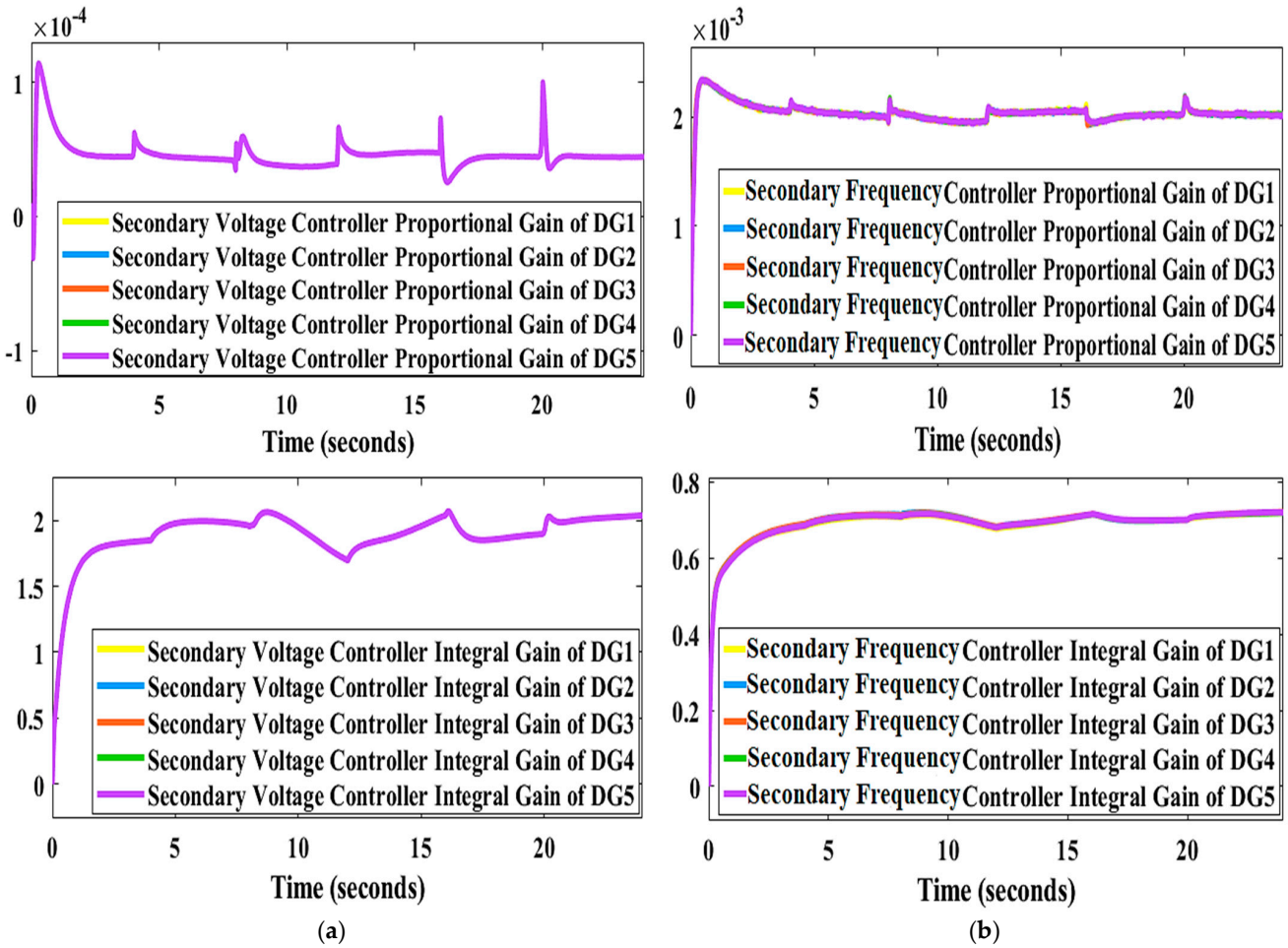


(**a**) (**b**)

**Figure 15.** Updating the voltage (**a**) and frequency (**b**) parameters of the SCUs in DGs under changing loading conditions.

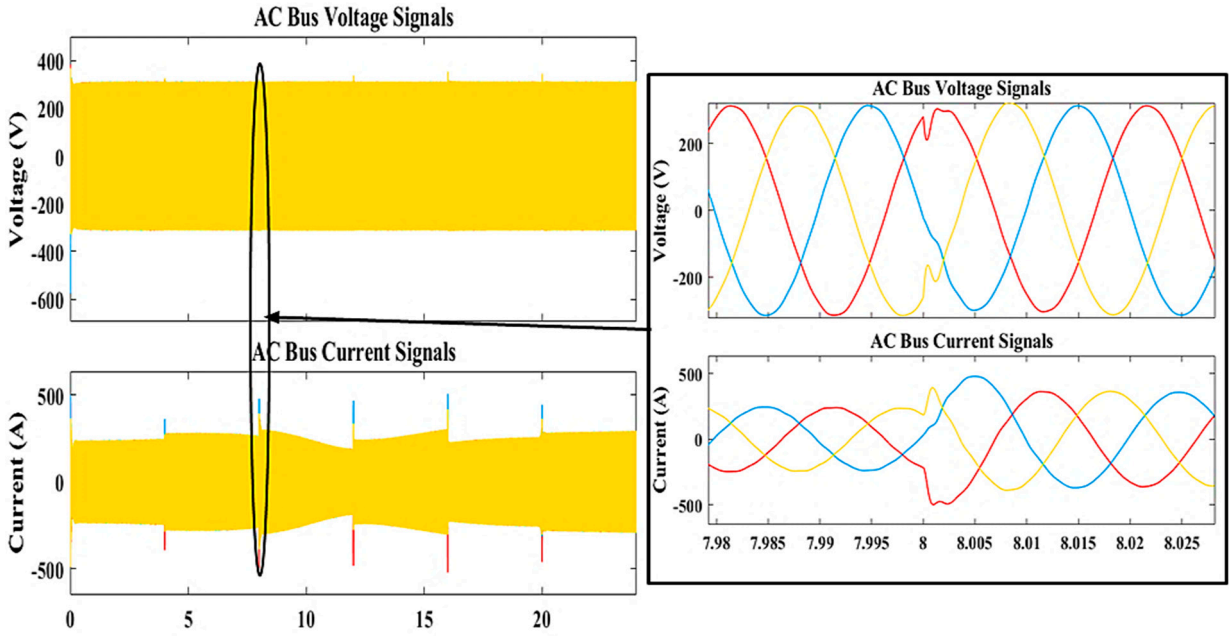


**Figure 16.** Three-phase voltage and current signals of AC bus.

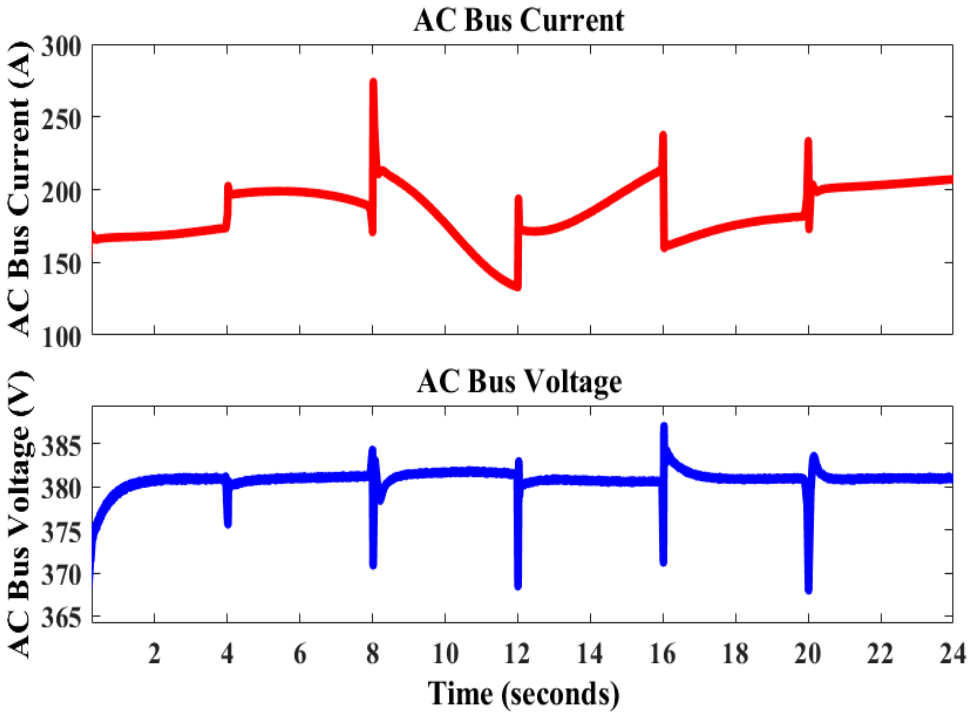


**Figure 17.** The root-mean-square line-to-line voltage and phase current of AC bus.

*7.3. System Power Losses Results*

Figure 18a,b shows power losses without and with EVB due to the impedances of the transmission lines. It is evident that EVB helps reduce losses during peak demand hours. The paper proposes a method for stabilizing frequency and voltage signals at their set points using ANNs with GA-optimized PI controllers, which modifies the parameters of the SCUs in all DGs in response to changes in operating points.

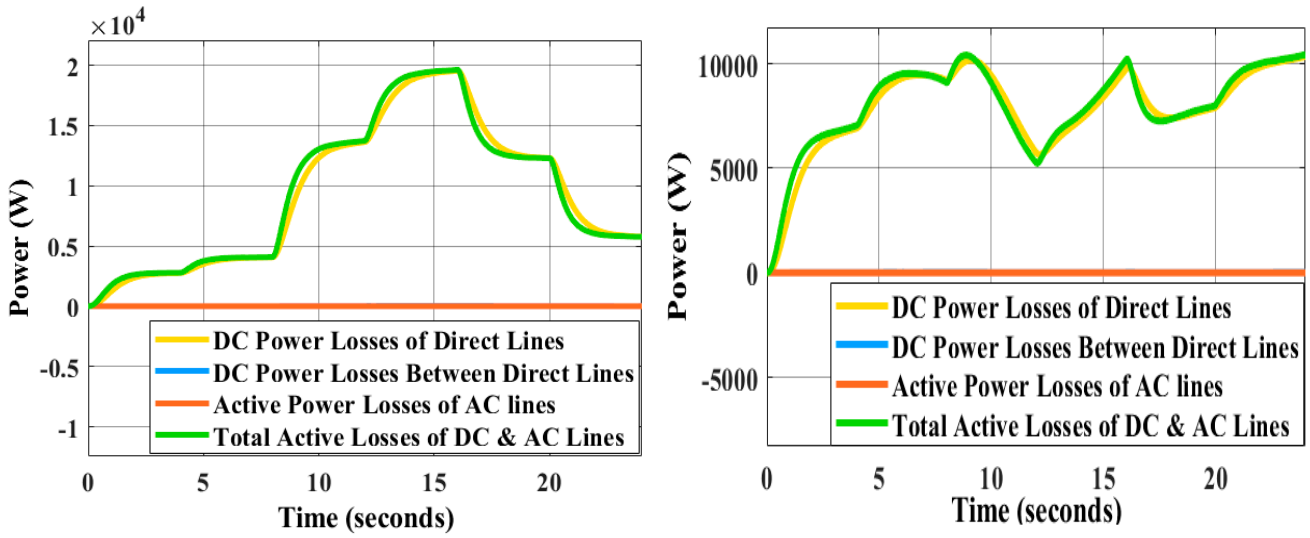


(**a**) (**b**)

**Figure 18.** System power losses under load conditions change (**a**) without EVB and (**b**) with EVB.

### *7.4. Energy Internet Platform Results*

As previously mentioned, the proposed real-time monitoring system was built on the ThingSpeak platform. The ThingSpeak toolbox in MATLAB/Simulink was used for cloud-based communication between the ThingSpeak platform and MATLAB/Simulink. As a result, the monitoring system enables building owners to view and oversee their properties from anywhere via the internet. Figure 19 illustrates the frequency and voltage responses of each DG on the ThingSpeak platform after the proposed control system strategy has been applied. There is no doubt that they are settled at their nominal values (50 Hz and 220 V). Every 15 s, the monitoring platform refreshes its results and shows the current variation from each source at the time the page was accessed. Figure 20a,b represents, respectively, the power generated by each DG and the total power production of the SG. If the price signal in Figure 21a is adopted, Figure 21b displays the total cost of electricity as it is displayed on the ThingSpeak platform.

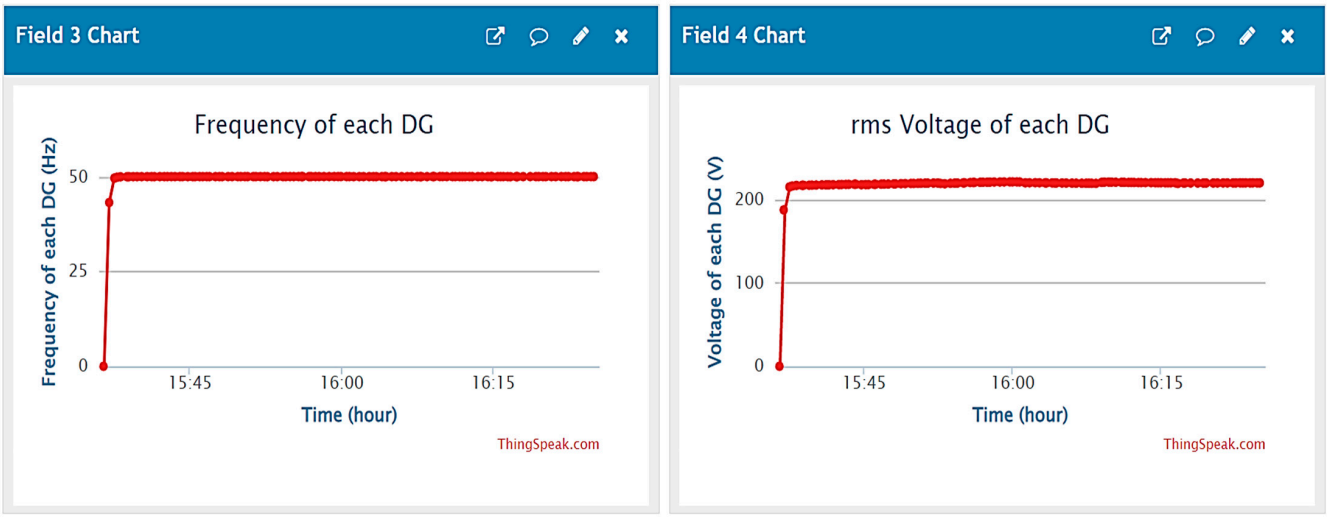


(**a**) (**b**)

**Figure 19.** (**a**) Frequency and (**b**) voltage responses using ThingSpeak platform.

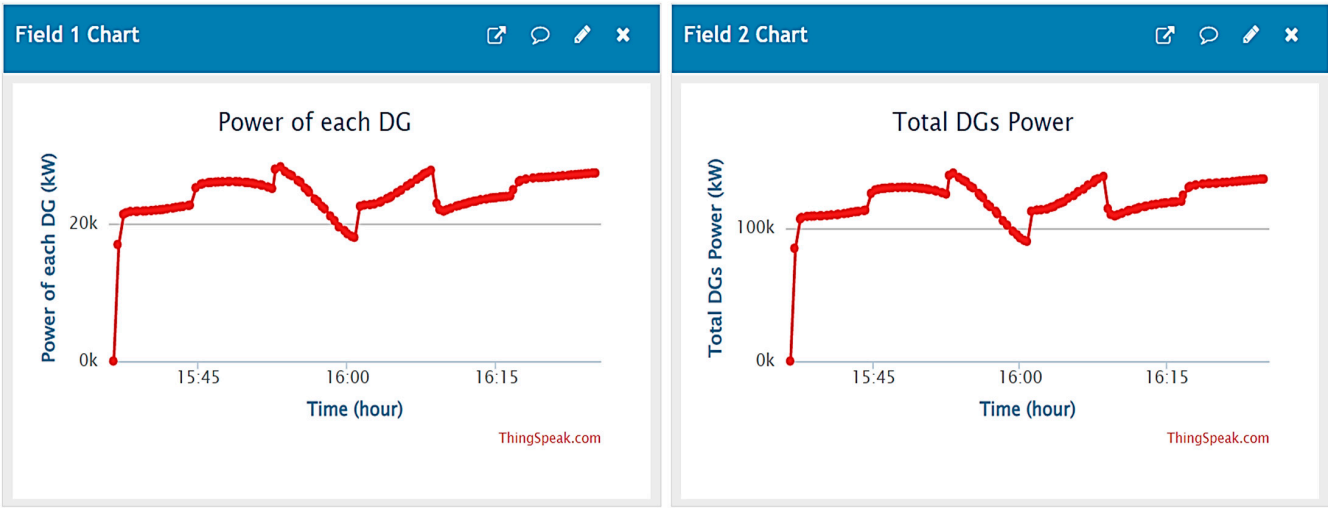


(**a**) (**b**)

**Figure 20.** (**a**) Power of each DG and (**b**) total SG power displayed by ThingSpeak platform.

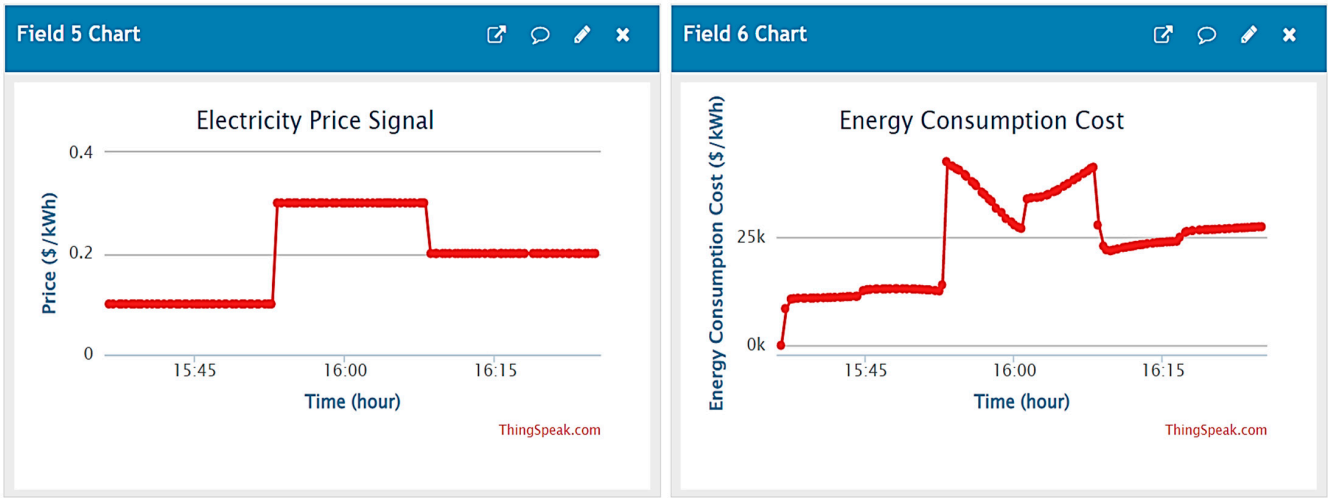


(**a**) (**b**)

**Figure 21.** (**a**) Adopted price signal and (**b**) total energy consumption cost displayed by ThingSpeak platform.

## 8. Conclusions

Since wind and solar energy are sporadic, RSs penetration exacerbates SG stability. DSM helps to fulfill demand when RSs power are inadequate. In this paper, a PLS DSM strategy based on storage systems is proposed to deal with this issue and make sure that SG's production and consumption are in balance. A new energy management system based on ANNs is proposed to improve the performance of SG-connected EVBs and meet load demand when RS power is scarce. This paper argues that charging stations in parking garages and other public areas can reduce energy use, especially at peak demand hours. ANNs have been combined with EVBs and DSM to achieve this goal. Based on the demand curve and EVB charge level, the proposed ANN controller can operate at specific times. The controller's inputs are time of day and SOC of EVB. Running the EVB during peak hours lowers the peak-to-average power ratio, allowing loads to operate more effectively. The suggested SG includes three solar PVs and two WTs. Distributed power-sharing control for DGs via virtual impedance-based adaptive primary control has also been presented. This study provides robust decentralized GA-based hierarchal secondary control to repair frequency and voltage discrepancies. In the proposed secondary control unit, a GA is used

to optimize all control parameters, while an ANN is used to better fine-tune controller parameters in an online manner. Moreover, DC transmission lines are adopted to transport electricity from RSs to connected inverters because they have low power losses, reduce reactive power concerns, increase grid performance, and prevent cascading blackouts. The simulation results are exhibited on both the MATLAB software and the Energy Internet ThingSpeak platform. The results show that each DG's voltage and frequency are stable at their nominal values (50 Hz and 220 volts), and parallel DGs share load power evenly regardless of variations in demand, thereby improving system stability, lowering energy costs, and enhancing the utility of the system for its users. The peak of total power losses may approach 20 kW without EVB-based demand management, but it can be reduced to 10 kW with the proposed EVB-based DSM.

The limitation of our work is that the control parameters are selected by integrating GA and ANNs in an online manner. This results in the system not always operating properly with a certain SG's configuration: for instance, in an AC-connected ring configuration of DGs, owing to the additional AC line impedances between any two DGs. By integrating offline optimization with consensus algorithm-based ANNs for online control parameter tweaking and exchanging information (voltage, frequency, and power) with each DG's local neighbors over a sparse cyber communication network, this issue may be handled in the future.

**Author Contributions:** A.M.J.: original draft, software, methodology, and validation; B.H.J.: supervisor, formal analysis; research resources; investigation; editing; and writing; and validation; B.-C.N. and S.A.: visualization; project administration; funding acquisition. All authors have read and agreed to the published version of the manuscript.

**Funding:** This research was funded by "Gheorghe Asachi" Technical University of Iasi, Romania.

**Institutional Review Board Statement:** Not applicable.

**Informed Consent Statement:** Not applicable.

**Data Availability Statement:** Not applicable.

**Conflicts of Interest:** The authors declare no conflict of interest.

## References

1. Jasim, A.M.; Jasim, B.H.; Bureš, V.; Mikulecký, P. A New decentralized robust secondary control for smart islanded microgrids. *Sensors* **2022**, *22*, 8709. [CrossRef]
2. Alhasnawi, B.N.; Jasim, B.H.; Esteban, M.D. A new robust energy management and control strategy for a hybrid microgrid system based on green energy. *Sustainability* **2020**, *12*, 5724. [CrossRef]
3. Jasim, A.M.; Jasim, B.H.; Kraiem, H.; Flah, A. A multi-objective demand/generation scheduling model-based microgrid energy management system. *Sustainability* **2022**, *14*, 10158. [CrossRef]
4. Alhasnawi, B.N.; Jasim, B.H.; Sedhom, B.E. Distributed secondary consensus fault tolerant control method for voltage and frequency restoration and power sharing control in multi-agent microgrid. *Int. J. Electr. Power Energy Syst.* **2021**, *133*, 107251. [CrossRef]
5. Jasim, A.M.; Jasim, B.H.; Mohseni, S.; Brent, A.C. Consensus-based dispatch optimization of a microgrid considering metaheuristic-based demand response scheduling and network packet loss characterization. *Energy* **2022**, *11*, 100212.
6. Åström, K.J.; Hägglund, T. Advanced PID control. *Instrum. Syst. Autom. Soc.* **2006**, *73*, 76–78.
7. Katiraei, F.; Iravani, M.; Lehn, P. Small-signal dynamic model of a micro-grid including conventional and electronically interfaced distributed resources. *IET Gener. Transm. Distrib.* **2007**, *1*, 369–378. [CrossRef]
8. Jasim, A.M.; Jasim, B.H.; Bures, V.; Mikulecky, P. A Novel Cooperative Control Technique for Hybrid AC/DC Smart Microgrid Converters. *IEEE Access* **2023**, *11*, 2164–2181. [CrossRef]
9. Han, Y.; Young, P.M.; Jain, A.; Zimmerle, D. Robust control for microgrid frequency deviation reduction with attached storage system. *IEEE Trans. Smart Grid* **2015**, *6*, 557–565. [CrossRef]
10. Mallesham, G.; Mishra, S.; Jha, A. Ziegler-Nichols based controller parameters tuning for load frequency control in a microgrid. In Proceedings of the 2011 International Conference on Energy, Automation, and Signal (ICEAS), Bhubaneswar, India, 28–30 December 2011; pp. 1–8.
11. Mallesham, G.; Mishra, S.; Jha, A. Maiden application of Ziegler-Nichols method to AGC of distributed generation system. In Proceedings of the Power Systems Conference and Exposition (PSCE'09), Seattle, WA, USA, 15–18 March 2009; pp. 1–7.

12. Jasim, A.M.; Jasim, B.H.; Neagu, B.-C.; Alhasnawi, B.N. Coordination control of a hybrid AC/DC smart microgrid with online fault detection, diagnostics, and localization using artificial neural networks. *Electronics* **2023**, *12*, 187. [CrossRef]
13. Dongol, D.; Feldmann, T.; Schmidt, M.; Bollin, E. A model predictive control based peak shaving application of battery for a household with photovoltaic system in a rural distribution grid. *Sustain. Energy Grids Netw.* **2018**, *16*, 1–13. [CrossRef]
14. Neves, S.A.; Marques, A.C.; Fuinhas, J.A. On the drivers of peak electricity demand: What is the role played by battery electric cars? *Energy* **2018**, *159*, 905–915. [CrossRef]
15. Jasim, A.M.; Jasim, B.H.; Neagu, B.-C.; Alhasnawi, B.N. Efficient optimization algorithm-based demand-side management program for smart grid residential load. *Axioms* **2022**, *12*, 33. [CrossRef]
16. Wong, L.A.; Ramachandaramurthy, V.K.; Taylor, P.; Ekanayake, J.; Walker, S.L.; Padmanaban, S. Review on the optimal placement, sizing and control of an energy storage system in the distribution network. *J. Energy Storage* **2018**, *21*, 489–504. [CrossRef]
17. Hu, T.; Ma, H.; Liu, K.; Sun, H. Lithium-ion battery calendar health prognostics based on knowledge-data-driven attention. *IEEE Trans. Ind. Electron.* **2022**, *70*, 407–417. [CrossRef]
18. Liu, K.; Peng, Q.; Teodorescu, R.; Foley, A.M. Knowledge-guided data-driven model with transfer concept for battery calendar ageing trajectory prediction. *IEEE/CAA J. Autom. Sin.* **2023**, *10*, 272–274. [CrossRef]
19. Kailong, L.; Zhongbao, W.; Chenghui, Z.; Yunlong, S.; Remus, T.; Qing-Long, H. Towards long lifetime battery: AI-based manufacturing and management. *IEEE/CAA J. Autom. Sin.* **2022**, *9*, 1139–1165.
20. Fathabadi, H. Novel wind powered electric vehicle charging station with vehicle-to-grid (V2G) connection capability. *Energy Convers. Manag.* **2017**, *136*, 229–239. [CrossRef]
21. Bhatti, A.R.; Salam, Z.; Sultana, B.; Rasheed, N.; Awan, A.B.; Sultana, U.; Younas, M. Optimized sizing of photovoltaic grid-connected electric vehicle charging system using particle swarm optimization. *Int. J. Energy Res.* **2018**, *43*, 500–522. [CrossRef]
22. Khan, S.U.; Mehmood, K.K.; Haider, Z.M.; Bukhari, S.B.A.; Lee, S.-J.; Rafique, M.K.; Kim, C.-H. Energy management scheme for an EV smart charger V2G/G2V application with an EV power allocation technique and voltage regulation. *Appl. Sci.* **2018**, *8*, 648. [CrossRef]
23. Mulla, A.; Jadhav, H.T. Optimal scheduling of vehicle-to-Grid power exchange using particle swarm optimization technique. *Int. J. Comput. Appl.* **2021**, *44*, 687–704. [CrossRef]
24. Shi, Y.; Xu, B.; Wang, D.; Zhang, B. Using battery storage for peak shaving and frequency regulation: Joint optimization for superlinear gains. *IEEE Trans. Power Syst.* **2018**, *33*, 2882e94. [CrossRef]
25. Kebede, A.A.; Coosemans, T.; Messagie, M.; Jemal, T.; Behabtu, H.A.; Van Mierlo, J.; Berecibar, M. Techno-economic analysis of lithium-ion and lead-acid batteries in stationary energy storage application. *J. Energy Storage* **2021**, *40*, 102748. [CrossRef]
26. Saffari, M.; de Gracia, A.; Fernández, C.; Belusko, M.; Boer, D.; Cabeza, L.F. Optimized demand side management (DSM) of peak electricity demand by coupling low temperature thermal energy storage (TES) and solar PV. *Appl. Energy* **2018**, *211*, 604–616. [CrossRef]
27. Krishan, O.; Suhag, S. An updated review of energy storage systems: Classification and applications in distributed generation power systems incorporating renewable energy resources. *Int. J. Energy Res.* **2019**, *43*, 6171–6210. [CrossRef]
28. Abbott, M.; Cohen, B. Issues associated with the possible contribution of battery energy storage in ensuring a stable electricity system. *Electr. J.* **2020**, *33*, 106771. [CrossRef]
29. Lange, C.; Rueß, A.; Nuß, A.; Öchsner, R.; März, M. Dimensioning battery energy storage systems for peak shaving based on a real-time control algorithm. *Appl. Energy* **2020**, *280*, 115993. [CrossRef]
30. Sridhar, V.; Umashankar, S.; Sanjeevikumar, P. Decoupled active and reactive power control of cascaded H-bridge PV-inverter for grid connected applications. In *Advances in Smart Grid and Renewable Energy*; Lecture Notes in Electrical Engineering; Springer: Berlin, Germany, 2018.
31. Kumuthawathe, A.; Rosnazri, A.; Taniselass, S. Battery energy storage system assessment in a designed battery controller for load leveling and peak shaving applications. *J. Renew. Sustain. Energy* **2017**, *9*, 044107.
32. Mao, T.; Xu, Q.; Zhou, B.; Zhang, R.; Wang, J. A load-based mechanism supporting peak shaving for Energy Storage (ES): An adaptive method. In Proceedings of the 2019 IEEE Sustainable Power and Energy Conference (iSPEC), Beijing, China, 21–23 November 2019. [CrossRef]
33. Sooyoung, J.; Yong, T.Y. Optimal operating schedule for energy storage system: Focusing on efficient energy management for microgrid. *Processes* **2019**, *7*, 80. [CrossRef]
34. Uddin, M.; Romlie, M.; Abdullah, M.; Tan, C.; Shafiullah, G.; Bakar, A. A novel peak shaving algorithm for islanded microgrid using battery energy storage system. *Energy* **2020**, *196*, 117084. [CrossRef]
35. Mulleriyawage, U.; Shen, W. Impact of demand side management on optimal sizing of residential battery energy storage system. *Renew. Energy* **2021**, *172*, 1250–1266. [CrossRef]
36. Simpson-Porco, J.W.; Dorfler, F.; Bullo, F. Synchronization and power sharing for droop-controlled inverters in islanded microgrids. *Automatica* **2013**, *49*, 2603–2611. [CrossRef]
37. Simpson-Porco, J.W.; Shafiee, Q.; Dorfler, F.; Vasquez, J.C.; Guerrero, J.M.; Bullo, F. Secondary frequency and voltage control of islanded microgrids via distributed averaging. *IEEE Trans. Ind. Electron.* **2015**, *62*, 7025–7038. [CrossRef]
38. Das, D.C.; Roy, A.; Sinha, N. GA based frequency 583 controller for solar thermal-diesel-wind hybrid energy gen584 eration/energy storage system. *Int. J. Electr. Power Energy Syst.* **2012**, *52*, 262–279. [CrossRef]

39. Al-Saedi, W.; Lachowicz, S.W.; Habibi, D.; Bass, O. Voltage and frequency regulation based DG unit in an autonomous microgrid operation using Particle Swarm Optimization. *Int. J. Electr. Power Energy Syst.* **2013**, *53*, 742–751. [CrossRef]
40. Vinayagam, A.; Abu Alqumsan, A.; Swarna, K.; Khoo, S.Y.; Stojcevski, A. Intelligent control strategy in the islanded network of a solar PV microgrid. *Electr. Power Syst. Res.* **2018**, *155*, 93–103. [CrossRef]
41. Alhasnawi, B.N.; Jasim, B.H.; Issa, W.; Anvari-Moghaddam, A.; Blaabjerg, F. A new robust control strategy for parallel operated inverters in green energy applications. *Energies* **2020**, *13*, 3480. [CrossRef]
42. Jasim, A.M.; Jasim, B.H. Grid-forming and grid-following based microgrid inverters control. *Iraqi J. Electr. Electron. Eng.* **2021**, *18*, 111–131. [CrossRef]
43. Jasim, A.M.; Jasim, B.H.; Aymen, F.; Kotb, H.; Althobaiti, A. Consensus-based intelligent distributed secondary control for multiagent islanded microgrid. *Int. Trans. Electr. Energy Syst.* **2023**, *2023*, 1–20. [CrossRef]
44. Zhi, D.; Xu, L. Direct power control of DFIG with constant switching frequency and improved transient performance. *IEEE Trans. Energy Convers.* **2007**, *22*, 110–118. [CrossRef]
45. Zhang1, C.; Zhou, Q.; Hua, M.; Wang, C.; Xu, H. Online double-layer system identification scheme for battery state-of-health prediction. In Proceedings of the International Conference on Applied Energy, Thailand/Virtual, 29 November–2 December 2021; Volume 24.
46. Yan, F.; Wang, J.; Du, C.; Hua, M. Multi-objective energy management strategy for hybrid electric vehicles based on TD3 with non-parametric reward function. *Energies* **2023**, *16*, 74. [CrossRef]
47. Jasim, A.M.; Jasim, B.H.; Neagu, B.-C. A new decentralized PQ control for parallel inverters in grid-tied microgrids propelled by SMC-based buck–boost converters. *Electronics* **2022**, *11*, 3917. [CrossRef]
48. Hachimi, H.; Ellaia, R.; El Hami, A. A new hybrid genetic algorithm and particle swarm optimization. *Key Eng. Mater.* **2012**, *498*, 115–125. [CrossRef]
49. Tiwari, M.K.; Vidyarthi, N. Solving machine loading problems in a flexible manufacturing system using a genetic algorithm based heuristic approach. *Int. J. Prod. Res.* **2000**, *38*, 3357–3384. [CrossRef]
50. Negnevitsky, M. *Artificial Intelligence: A Guide to Intelligent Systems*, 2nd ed.; Pearson: New York, NY, USA, 2005.
51. Liu, K.; Peng, Q.; Sun, H.; Fei, M.; Ma, H.; Hu, T. A transferred recurrent neural network for battery calendar health prognostics of energy-transportation systems. *IEEE Trans. Ind. Inform.* **2022**, *18*, 8172–8181. [CrossRef]
52. Liu, K.; Peng, Q.; Che, Y.; Zheng, Y.; Li, K.; Teodorescu, R.; Widanage, D.; Barai, A. Transfer learning for battery smarter state estimation and ageing prognostics: Recent progress, challenges, and prospects. *Adv. Appl. Energy* **2023**, *9*, 100117. [CrossRef]